Contents lists available at ScienceDirect

Remote Sensing of Environment

OCO-3 early mission operations and initial (vEarly) XCO_2 and SIF retrievals

Thomas E. Taylor[a,*], Annmarie Eldering[b], Aronne Merrelli[c], Matthäus Kiel[b], Peter Somkuti[a], Cecilia Cheng[b], Robert Rosenberg[b], Brendan Fisher[b], David Crisp[b], Ralph Basilio[b], Matthew Bennett[b], Daniel Cervantes[b], Albert Chang[b], Lan Dang[b], Christian Frankenberg[d], Vance R. Haemmerle[b], Graziela R. Keller[b], Thomas Kurosu[b], Joshua L. Laughner[d], Richard Lee[b], Yuliya Marchetti[b], Robert R. Nelson[b], Christopher W. O'Dell[a], Gregory Osterman[b], Ryan Pavlick[b], Coleen Roehl[d], Robert Schneider[b], Gary Spiers[b], Cathy To[b], Christopher Wells[b], Paul O. Wennberg[d], Amruta Yelamanchili[b], Shanshan Yu[b]

[a] Cooperative Institute for Research in the Atmosphere, Colorado State University, Fort Collins, CO 80521, USA
[b] Jet Propulsion Laboratory, California Institute of Technology, Pasadena, CA 91109, USA
[c] Space Science and Engineering Center, University of Wisconsin - Madison, Madison, WI 53706, USA
[d] California Institute of Technology, Pasadena, CA, USA

ARTICLE INFO

ABSTRACT

NASA's Orbiting Carbon Observatory-3 (OCO-3) was installed on the International Space Station (ISS) on 10 May 2019. OCO-3 combines the flight spare spectrometer from the Orbiting Carbon Observatory-2 (OCO-2) mission, which has been in operation since 2014, with a new Pointing Mirror Assembly (PMA) that facilitates observations of non-nadir targets from the nadir-oriented ISS platform. The PMA is a new feature of OCO-3, which is being used to collect data in all science modes, including nadir (ND), sun-glint (GL), target (TG), and the new snapshot area mapping (SAM) mode.

This work provides an initial assessment of the OCO-3 instrument and algorithm performance, highlighting results from the first 8 months of operations spanning August 2019 through March 2020. During the In-Orbit Checkout (IOC) phase, critical systems such as power and cooling were verified, after which the OCO-3 spectrometer and PMA were subjected to a series of rigorous tests. First light of the OCO-3 spectrometer was on 26 June 2019, with full science operations beginning on 6 August 2019. The OCO-3 spectrometer on-orbit performance is consistent with that seen during preflight testing. Signal to noise ratios are in the expected range needed for high quality retrievals of the column-averaged carbon dioxide (CO_2) dry-air mole fraction (XCO_2) and solar-induced chlorophyll fluorescence (SIF), which will be used to help quantify and constrain the global carbon cycle.

The first public release of OCO-3 Level 2 (L2) data products, called "vEarly", is being distributed by NASA's Goddard Earth Sciences Data and Information Services Center (GES DISC). The intent of the vEarly product is to evaluate early mission performance, facilitate comparisons with OCO-2 products, and identify key areas to improve for the next data release. The vEarly XCO_2 exhibits a root-mean-squared-error (RMSE) of $\simeq$ 1, 1, 2 ppm versus a truth proxy for nadir-land, TG&SAM, and glint-water observations, respectively. The vEarly SIF shows a correlation with OCO-2 measurements of > 0.9 for highly coincident soundings. Overall, the Level 2 SIF and XCO_2 products look very promising, with performance comparable to OCO-2. A follow-on version of the OCO-3 L2 product containing a number of refinements, e.g., instrument calibration, pointing accuracy, and retrieval algorithm tuning, is anticipated by early in 2021.

1. Introduction

OCO-3 was launched to the International Space Station (ISS) from Kennedy Space Center, Florida on 4 May 2019 at 06:48 UTC on a Space-X Falcon 9 rocket. The Dragon capsule docked with ISS on 6 May 2019 and the OCO-3 instrument was extracted from the Dragon trunk 3 days

---

later (9 May 2019) and installed on the Japanese Experiment Module Exposed Facility (JEM-EF) on 10 May 2019. OCO-3 completed its 90 day In-Orbit Checkout (IOC) and began collecting science measurements on 6 August 2019 (orbit, or" solar day" number 1456).

OCO-3 uses the flight spare spectrometer from the OCO-2 mission, which has been taking data from a 705-km altitude, near-polar, sun-synchronous orbit since September 2014 (Crisp et al., 2017). Like the OCO-2 instrument, the OCO-3 spectrometer includes three spectral channels, centered on the molecular oxygen-A band (ABO2) at 0.765 μm and the two CO_2 bands at 1.61 μm (WCO2) and 2.06 μm (SCO2). With a nominal mission lifetime of 3 years (through mid 2022), the primary science objective of the OCO-3 mission is to provide high precision, spatially-resolved, global measurements of the dry-air mole fraction of column carbon dioxide (XCO_2) from space (Eldering et al., 2019a). As with OCO-2, OCO-3 will also provide estimates of the solar-induced fluorescence (SIF) via measurements in the ABO2 channel (Frankenberg et al., 2014; Sun et al., 2018).

For nominal science operations, OCO-3 collects down-looking (nadir viewing) measurements over land (abbreviated NL) and observations near the specular glint spot over water (abbreviated GW) to maximize the observed signal. Unlike for OCO-2, where the spacecraft reorients to point the instrument, the OCO-3 instrument uses an agile 2-D pointing mirror assembly (PMA) to point toward the ocean glint spot or stationary surface targets (abbreviated TG), from the nadir-pointing ISS platform. The PMA also enables the acquisition of snapshot area maps (SAMs) to yield spatially-resolved 2-D images ($\simeq 85 \times 85$ km) of local hot-spot emissions and other sites of interest such as instrumented field stations.

The low-inclination, precessing orbit of the ISS allows OCO-3 to sample the spatial and temporal distribution of XCO_2 and SIF quite differently than the repeating, sun synchronous orbit of OCO-2 (Eldering et al., 2019a). ISS overpasses do not occur at the same local time of day for a given latitude. Instead, the overpass time is approximately 20 min earlier each day, eventually sampling all times of day from dawn to dusk. Thus, OCO-3 is providing new information on the diurnal variations in XCO_2 and SIF and their implications for the carbon cycle. A few key comparisons and contrasts between OCO-2 and OCO-3 are provided in Table 1.

This paper describes the early operations of OCO-3 and the first public release of the OCO-3 data products - version "vEarly". This version of the data used the newest Atmospheric Carbon Observations from Space (ACOS) build 10 (b10) software suite (Eldering et al., 2019b; Boesch et al., 2019; Osterman et al., 2020), which includes meteorology, preprocessors, SIF, and XCO_2 from the L2FP retrieval algorithm. These data products are being distributed by the NASA's Goddard Earth Sciences Data and Information Services Center (GES DISC). The intent of the vEarly products is to evaluate early mission performance, facilitate comparisons with OCO-2, and identify the key areas to improve for the next data release. A follow-on version of the OCO-3 data, v10, also using the b10 software suite, will contain a number of refinements including instrument calibration, pointing

accuracy, and retrieval algorithm tuning. OCO-3 v10 is anticipated to be released to the public by early in 2021.

The paper is organized as follows. Section 2 begins with a description of activities performed during the IOC phase of the mission, provides a summary of the observation modes of OCO-3, and concludes with an overview of early science operations, with additional details given in Appendix A. Section 3 provides some early validation and analysis of the Level 2 (L2) preprocessors used for clear-sky sounding selection. Section 4 examines the time of day and sampling density of OCO-3 vEarly, and characterizes the Level 1B (L1B) data. Section 5 provides an initial overview of L2 SIF retrievals, and Section 6 explores initial L2 Full Physics (L2FP) retrieval performance, including the bias correction and quality filters used for the vEarly data release. In Sections 3 through 6 direct comparisons with OCO-2 over the same time period are made. Finally, Section 7 summarizes the overall performance of the early OCO-3 operations and the vEarly data products, spanning August 2019 through March 2020. For convenience, a table of frequently used acronyms and abbreviations is given in Table 2.

2. OCO-3 early mission calibration, observing modes, and science operations

2.1. In-Orbit Checkout (IOC)

Critical systems, including communications, power and cooling, were checked out immediately after instrument installation on 10 May 2019 and found to be operating nominally. The PMA functionality was then verified and the initial PMA calibration activity commenced. The spectrometer focal plane array (FPA) detectors and optical bench assembly (OBA) were maintained near room temperature to accelerate out-gassing over a 3-week decontamination (decon) cycle. The spectrometer FPA and OBA were then cooled to their operating temperatures and first light spectra were acquired on 26 June 2019. Additional early mission check-out and calibration activities were also completed during IOC.

2.1.1. Context cameras

Unlike the OCO-2 instrument, OCO-3 is equipped with both internal and external context cameras, based on an existing compact, rugged JPL design appropriate for use on the ISS (McKinney et al., 2018). These cameras were primarily intended to aid in geolocation calibration, but they also provide qualitative information useful for reviewing cloud screening and spatial coverage of SAM and target measurements.

The internal context camera (ICC) is a monochromatic camera that is co-boresighted with the OCO-3 spectrometer. It is located inside the PMA, just before the instrument aperture, with a small pick-off mirror allowing the same beam of light that reaches the instrument to be directed into the camera. The native readout is a 4480 × 3840 image, which has been windowed to 640 × 640, 320 × 320, and 300 × 300 at various times in the early mission. However, the PMA bore-sight reduces this to a circular image of approximately 460 pixel diameter, or

Table 1
Comparing and contrasting key characteristics of the OCO-2 and OCO-3 platforms.

	OCO-2	OCO-3
Orbit description	Low-Earth sun-synchronous polar	Low-Earth precessing
Orbit inclination	98.2°	51.6°
Orbit period	98.82 min	90–93 min (depending on ISS altitude)
Overpass time	$\simeq$ 13:30 local with a $\simeq$ 2 h latitudinal gradient	Varies ~ ± 5 h from local solar noon across a 66 day illumination cycle
Footprint size (cross-track)	< 1.3 km	< 1.6 km
Footprint size (along-track)	$\simeq$ 2.3 km (at nadir)	$\simeq$ 2.2 km (at nadir)
Footprint area	$\simeq$ 3.0 km^2 (at nadir)	$\simeq$ 3.5 km^2 (at nadir)
Pointing control	Orientation of the satellite bus	2-axis Pointing Mirror Assembly
Observation modes	Nadir, Glint, Target	Nadir, Glint, Target and Snapshot Area Mapping
Observation frequency	3 Hz	3 Hz
Footprints per frame	8	8

Table 2

Acronyms and abbreviations used throughout the paper.

Acronym/Abbrev.	Description	Notes
ABP	A-Band Preprocessor	A computationally fast algorithm used for clear-sky sounding selection.
AGP	Ancillary Geometric Product	OCO-2/3 calibration file containing essential parameters used for geolocating soundings.
ARP	Ancillary Radiometric Product	OCO-2/3 calibration file containing essential parameters used for calibrating measured spectra.
ABO2	Molecular oxygen A-Band channel	The spectral channel sampling the 0.765 μm molecular oxygen A-Band (O_2 A-Band), cloud and aerosol optical properties and SIF.
AZ	AZimuth	PMA azimuth angle. Used to characterize the OCO-3 polarization angle.
BAD	Broadcast Ancillary Data	1 Hz ISS telemetry supplied to all instruments on the ISS.
BPM	Bad Pixel Map	OCO-2/3 calibration parameters that identify individual pixels on the FPA that are identified as faulty. Updates are made through the FSW.
COCCON	Collaborative Carbon Column Observing Network	A network of ground field stations equipped with EM27/SUN Fourier transform spectrometers used to validate space-based measurements of XCO2.
ECC	External Context Camera	Mounted outside the spectrometer box. Provides images $\simeq$100 $\times$ 100 km, roughly the size of a SAM.
EL	ELevation	PMA elevation angle. Used to characterize the OCO-3 polarization angle.
FOV	Field of View	The projection on the ground of the OCO-2/3 spectrometers.
FPA	Focal Plane Array	The array of light sensing pixels specific to each OCO spectrometer (1024 $\times$ 1024).
FSW	Flight SoftWare	The on-board software used to control OCO-3. Updates can be uploaded from the HOSC.
GASBAG	Generic Algorithm for Single Band Acquisition of Gases	A new, computationally fast algorithm used for both clear-sky sounding selection and retrieval of SIF.
GL, GW	Glint-Land, Glint-Water	Glint is one of the primary measurement modes of OCO-2/3, in which the spectrometer boresight is pointed close to the specular glint spot. Used mainly over water to achieve high SNR.
GPS	Global Positioning System	ISS GPS data was used to validate the OCO-3 IMU and SRU data during IOC.
HFLN	Hours From Local Noon	A time-of-day metric used for assessing the OCO-3 data.
HOSC	Huntsville Operations Support Center	Operations center for the ISS, located at NASA's Marshall Space Flight Center (MSFC) in Huntsville, Alabama.
ICC	Internal Context Camera	Camera located inside the PMA, just before the instrument aperture. Provides bore sighted images with a FOV $\simeq$40 km. Used for PMA calibration.
IDP	IMAP-DOAS Preprocessor	A computationally fast algorithm used for both clear-sky sounding selection and retrieval of SIF.
IOC	In-Orbit Checkout	Ninety day period following launch in which critical systems and spectrometer performance are assessed.
IMU	Inertial Measurement Unit	A subsystem consisting of gyros and accelerometers that measure velocity and attitude changes of the ISS needed for accurate PMA operation.
ISS	International Space Station	Platform from which OCO-3 will operate for a nominal 3 year mission.
L2FP	Level 2 Full Physics algorithm	The primary retrieval algorithm used to estimate the dry-air mole fraction of carbon dioxide from space-based measurements of reflected solar radiation.
MOS	Mission Operations System	OCO-3 project level mission operations.
NL, NW	Nadir-Land, Nadir-Water	Nadir viewing is one of the primary measurement modes of OCO-2/3, in which the spectrometer boresight is pointed (nearly) straight down. Primarily used over land to minimize the chance of cloud contamination.
OCO	Orbiting Carbon Observatory	OCO-2 was launched into a polar orbit in July 2014. OCO-3 was installed on the ISS in May 2019.
PCS	Pointing Control Software	The MOS software used to direct the PMA.
PMA	Pointing Mirror Assembly	External 2-axis pointing system used to control OCO-3 spectrometer ground field of view.
SAM	Snapshot Area Map	An observation mode specific to OCO-3 used to target areas of interest, such as fossil fuel emission sources, volcanoes and field research/validation sites. Typical collection size is $\simeq$ 80 $\times$ 80 km.
SCO2	Strong Carbon Dioxide channel	The spectral channel sampling the 2.06 μm "strong" CO_2 spectral band used for retrieving carbon dioxide.
SIF	Solar Induced chlorophyll Fluorescence	Radiation emitted by plants in the O_2-A band as a result of photosynthesis that is detectable from space.
SRU	Stellar Reference Unit	A subsystem that uses fixed positions of stars to measure velocity and attitude changes of the ISS needed for accurate PMA operation.
SZA	Solar Zenith Angle	Angle of the sun in the sky measured as zero degrees at nadir and ninety degrees on the horizon.
TCCON	Total Carbon Column Observing Network	A network of ground field stations equipped with instruments calibrated to the WMO CO_2 standard used to validate space-based measurements of XCO2.
TG	Target	One of the auxiliary measurement modes of OCO-2/3, in which the spectrometer bore sight is "targeted" to a specific ground location. Used primarily at TCCON validation sites.
WCO2	Weak Carbon Dioxide channel	The spectral channel sampling the 1.61 μm "weak" CO_2 spectral band used for retrieving carbon dioxide.
XCO_2	Column-averaged dry-air mole fraction of carbon dioxide	The primary science product of the OCO-2/3 missions.

approximately four times the diameter of a single $\simeq$ 10 km spectrometer FOV. Individual pixels have an 0.22 mrad FOV, which provides 88 m ground resolution at nadir at the ISS orbit altitude. ICC images were collected every 4 s during IOC and PMA calibration activities.

The external context camera (ECC) is a three-band (colour) camera mounted outside the spectrometer box, on the end of the pointing mirror assembly. To reduce the down-link data volume, the ECC is windowed to 2223 $\times$ 2220 pixels (277.8 $\times$ 277.5 mrad). Three rows/columns are combined to reduce the image size to 741 $\times$ 740 pixels, each with an effective angular resolution of 0.375 mrad, yielding a 150 m per pixel ground resolution at nadir. The overall image covers $\simeq$ 115 km $\times$ 115 km, which is about twice the dimension of a Snapshot Area Map (SAM). An ECC image is collected every 15 s.

Images acquired by the context cameras on 17 May 2019 over the Andes Mountains are shown in Fig. 1. Early in the mission both cameras were used extensively, but in routine operations only the external

camera collects data. Currently, the data are only used internally at JPL for calibration of the PMA (refer to Section 2.1.2) and to assist in non-automated cloud screening of SAM and target measurements.

2.1.2. Pointing mirror assembly (PMA) calibration

The PMA pointing geometry was characterized and calibrated in pre-flight testing. Once in orbit, it was anticipated that the PMA would need to be re-calibrated due to uncertainties in the exact installation geometry on the ISS, gravity release, timing errors in FSW, and limitations in the pointing control system (PCS). In-flight pointing and geolocation updates were executed in two phases. First, the payload systems that provide PCS with time and position information (Global Positioning System (GPS), stellar reference unit (SRU), and inertial measurement unit (IMU)) were calibrated and their performance was verified. These tests revealed errors in the time data that was being passed to FSW. These errors were typically less than 1 s, but contributed
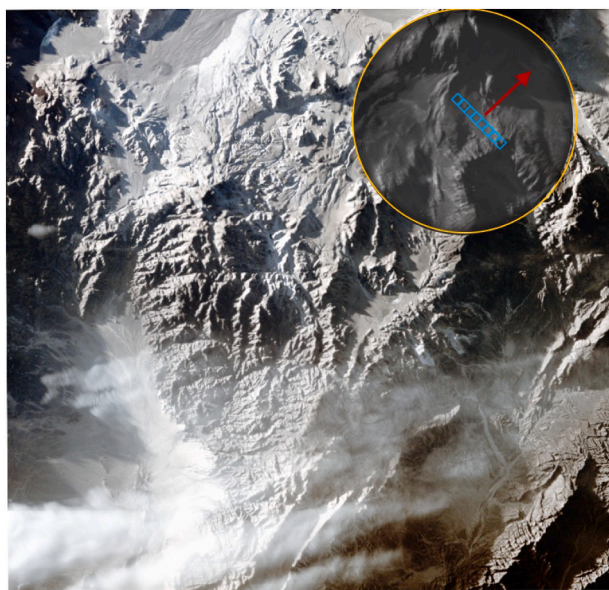
Fig. 1. OCO-3 external context camera image acquired on 17 May 2019 over the Andes mountains. An overlay of a circular ICC image, designated with a gold border, is shown in the upper right. A single OCO-3 measurement frame is shown in blue for context and the direction of ISS/OCO-3 flight is indicated by the red arrow. (For interpretation of the references to colour in this figure legend, the reader is referred to the web version of this article.)

substantially to the total geolocation error since the ISS travels at $\simeq$ 7.7 km/s. As a workaround for this timing error, the payload was operated with the ISS Broadcast Ancillary Data (BAD) as the source of timing and position data for the pointing control software for much of the early mission. Because these data are collected by systems located at the center of the ISS, they are not an exact representation of OCO-3's position, but the difference can be estimated. After an update to the flight software (FSW) to version v4.2 on 29 Oct 2019, the timing errors were significantly reduced, and the focus then shifted to other sources of errors in geolocation.

With reduced timing errors, the remaining potential source of error is the understanding of the mounting of the pointing mirror system and position-dependent mis-characterizations of the PMA position. To characterize position dependent errors of the PMA, and to develop a correction table, a pointing mirror assembly (PMA) calibration activity (PMACal) was conducted. In this activity, images were collected with the ICC while the PMA was moved through a grid of azimuth (AZ) and elevation (EL) positions. The ICC images were compared to reference

Landsat images sampled with the position information from the payload (Bryant et al., 2012). Image processing tools were used to define ground control points and determine the AZ and EL shifts needed to optimize the image registration. Once a grid of AZ/EL corrections was developed from the ICC images, a simplified payload model was used to determine parameters such as AZ/EL offset, scale factors, and mirror misalignment terms. The model was optimized to minimize the difference from the AZ/EL offsets determined from PMACal and those predicted from the model. The model best fit was used to generate a gridded AZ/EL correction table. This correction table was uploaded to the payload, and when the PCS determines an AZ/EL position to point to a desired location, it is then adjusted by the offsets, so that the actual measurement location matches the desired location.

The PMACal activities were completed in November 2019 and the first version of a correction table was uploaded on 17 December 2019. The PMA correction table was also used in the ground data processing system to improve the geolocation knowledge for data collected prior to the creation of the updated table. A detailed assessment of the data collected after the FSW v4.2 upload and the PMACal images revealed another small timing error in the PCS system, which results in a pointing error of about 400 m ($1/5^{th}$ of a footprint). In addition, an interpolation error in the PCS system introduces a small jitter in the footprint geolocation. While these are small errors, they can be overcome by using the ISS back-queried BAD as the position and ephemeris data. The team uses the PCS data for forward processing, as it is immediately available, and relies on the back queried BAD for retrospective processing.

2.1.3. Residual pointing error

A second version of the pointing correction table, using a larger set of ICC images, was uploaded in March 2020. Data evaluated at coastlines (see Fig. 2) shows that current pointing errors are smaller than a single OCO-3 footprint in nadir viewing mode. However, SAM and target data collected at a larger range of PMA AZ and EL positions have larger residual errors. These have been analyzed by evaluating three metrics: (1) differences between the a priori surface pressure and the values retrieved from the A-band Preprocessor (ABP); (2) the XCO_2 from a WCO2-only single band retrieval and (3) difference between the retrieved and MODIS surface albedo. The best-fit pointing offsets are calculated by shifting the data geolocation on a fine latitude and longitude grid to minimize differences (or the standard deviation in the case of XCO_2) relative to the reference values.

Using this approach, the residual errors are found to be smallest at small positive EL positions (looking in the direction of flight), and largest at large negative EL positions (looking opposite the direction of flight). They appear to be on the order of 1 km for many positions, but can grow to about 4 km at the larger EL positions, and appear to have
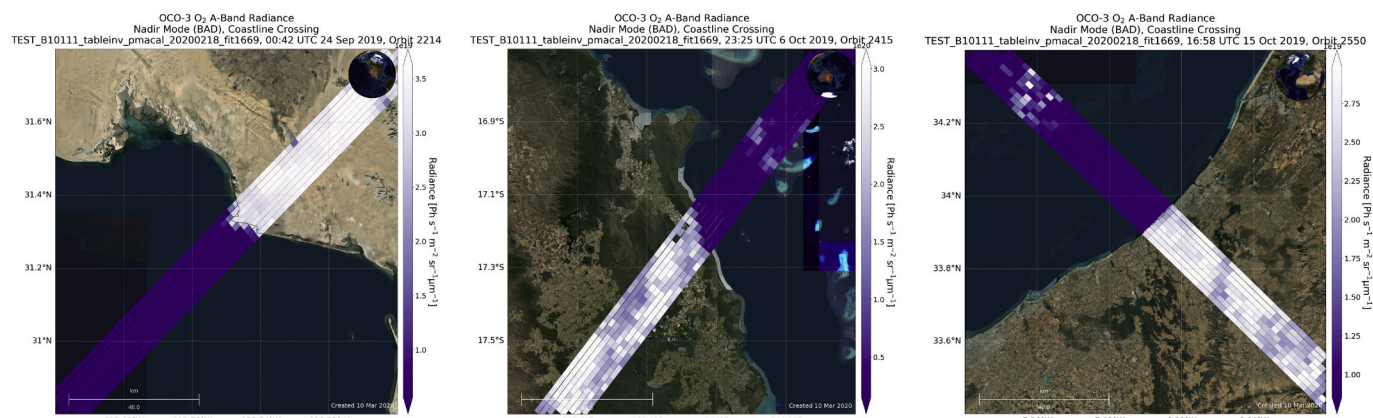
Fig. 2. Examples of three coastline crossings colored by radiance level in the ABO2 spectral band. The dark colors indicate low radiances over water surfaces observed in nadir geometry. These illustrate the remaining pointing error for nadir, which is on the order of a footprint, but variable in time.

some variation in time. The team is investigating possible explanations, including additional timing errors, errors in the mounting angles, and remaining errors in the PMACal correction table. Another potential source of error is the use of the BAD data, which is derived from measurements at the center of the ISS, the orientation or attitude of which may vary over time relative to the OCO-3 payload position. Once the source of the error is determined, it will be corrected and applied to the next data reprocessing effort.

2.1.4. Spectrometer calibration and performance

Prior to launch, the OCO-3 instrument underwent extensive calibration in a thermo-vacuum chamber. Results from these tests were used to derive the at-launch versions of the Ancillary Radiometric Product (ARP), containing radiometric and spectral calibration coefficients and the Ancillary Geometric Product (AGP), containing the centroids and widths of each spatial footprint. The AGP also contains the parameters to relate the internal context camera position to the instrument slit. Once in orbit, only a few of these calibration parameters can be updated. For radiometric calibration, these include the dark calibration, linear scaling of the radiometric gains, and a stray light correction. For spectroscopic calibration, the spectral dispersion can be evaluated using the gas absorption line positions in the science data, and can be modified by shifting or stretching the wavelength scale. Recently, the first in a series of papers describing pre-flight calibration was published (Marchetti et al., 2019).

A key milestone in the operation of any satellite spectrometer is acquiring what is known as "first light" - the first set of measurements that are made with the instrument FPAs cooled to operating temperatures and all other systems in nominal measurement mode. The first nadir-land (NL) overpass for OCO-3 occurred on 26 June 2019 over the United States, passing from the northern Pacific, southeastward, to the Gulf of Mexico. A set of spectra, acquired over northern Texas are shown in Fig. 3. The first light spectra show the expected molecular absorption features and continuum levels in each band.

In-flight calibration data collection for OCO-3 includes dark data, lamp measurements, and vicarious calibration at ground sites. OCO-3 has a custom calibrator designed to interface with the PMA. It contains three lamps, identical to those used on OCO-2, but with a different diffuser. The primary lamp (lamp #3) is used on almost every orbit, roughly a dozen times each day. The secondary lamp (lamp #2) is used three times per day, and the tertiary lamp (lamp #1) is used once per week. Dark data are acquired as often as 40 times daily with the PMA in the same position, but with the lamps off.

From an on-orbit calibration perspective, the most significant difference between OCO-2 and OCO-3 on the ISS is the lack of solar calibration for OCO-3, as the system does not include a solar diffuser and the viewing constraints do not allow the pointing system to view the Sun. Another key difference is that the field of view of the spectrometer optics was made 2.2 times larger to maintain surface footprint sizes similar to those of OCO-2, which operates from a significantly higher altitude orbit ($\simeq$450 km for the ISS versus $\simeq$705 km for OCO-2). This required modifications to the light sources used in ground testing and complicated the analysis because the sources were less uniform within the instrument's field of view. Detailed results from the pre-launch testing will be published in a forthcoming calibration paper. One benefit of operations aboard the ISS is more frequent data downlinks that enable a larger volume of calibration data when there is a sufficiently long eclipse of the sun. However, that is balanced by varying eclipse lengths with the precessing orbit as well as more frequent operational disruptions.

An unexpected discovery during IOC was that all three lamps had brightened relative to their prelaunch levels. At first light, the increase in the primary calibration lamp, the only one used for radiometric calibration of vEarly, was $\simeq$ 15.3% for the ABO2, $\simeq$ 8.2% for the WCO2,
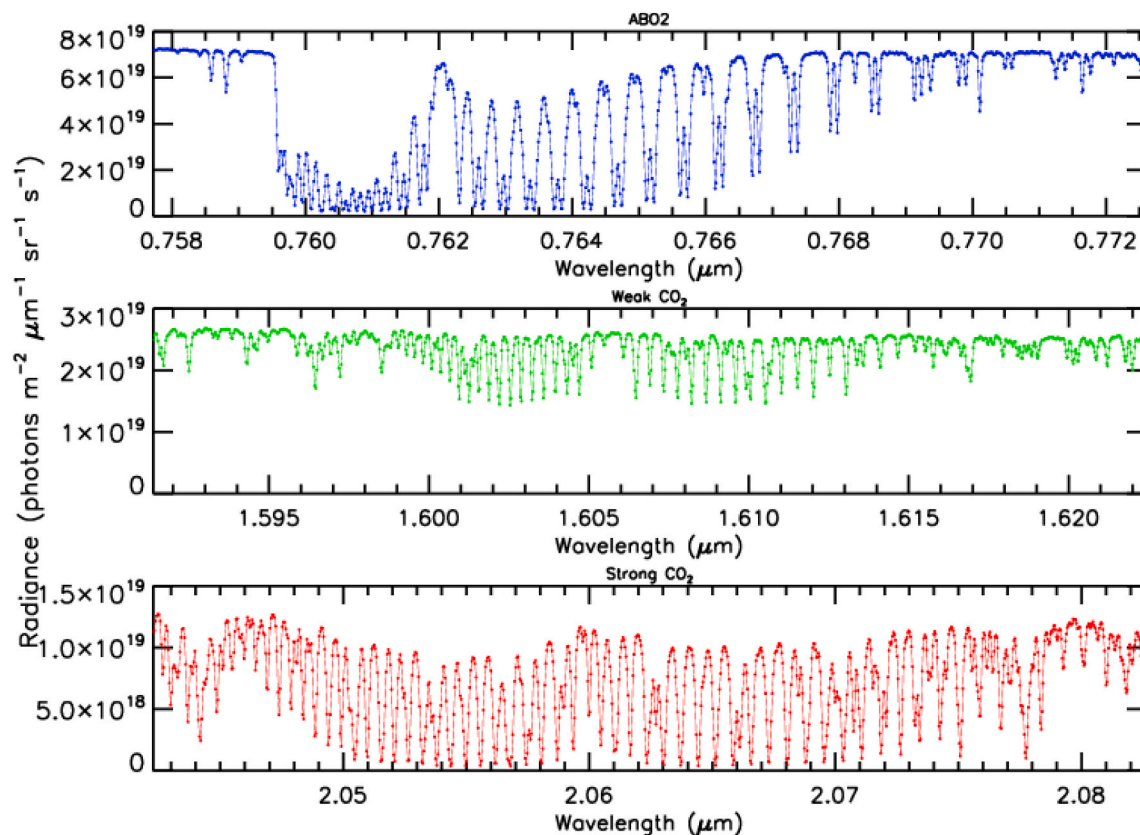

Fig. 3. OCO-3 first light spectra acquired on 26 June 2019 over north Texas. Oxygen-A band (top), Weak CO_2 band (middle) and Strong CO_2 band (bottom). Each pixel in the spectra is marked by a circle, illustrating how the absorption features are sampled.

and $\simeq 7.4\%$ for the SCO2. The relative brightening of the three bands suggests a small colour temperature shift of $\simeq 1.5\%$ from a baseline value near 2700 K. To derive in-flight gain degradation, the primary lamp radiance trend is adjusted by these scale factors and then corrected by a linear fit with time. This approach does not capture lamp aging, which will be constrained in future releases by (i) inter-comparing the three on-board lamps, (ii) performing on-board lunar calibration, (iii) analysing surface targets (Yu et al., 2020), and (iv) making direct comparisons to OCO-2.

A key calibration milestone during IOC was an update of the bad pixel map (BPM), which identifies the pixels on each FPA that are dead or perform anomalously and cannot be calibrated. On OCO-2, which used flight spare FPAs from the OCO mission that were manufactured in 2006, a significant number of new bad pixels developed on the WCO2 and SCO2 FPAs between pre-flight testing and IOC. This required four updates to the BPM in the first 6 months of operations. Even after that, the tracking and removal of outliers remains a significant challenge. Fortunately, OCO-3 uses updated FPAs in these two spectral channels and developed far fewer new bad pixels. In addition, a new machine learning tool was recently developed to identify bad pixels more quickly (Marchetti et al., 2019). The latest bad pixel map for OCO-3, designated BPM 103, was uploaded on orbit 1285, 26 July 2019.

The OCO-3 project delivers both forward and retrospective data product streams, as is done for OCO-2. The forward stream generates calibrated radiance spectra using extrapolated estimates of the calibration coefficients, based on recent trends in the FPA and OBA thermal environment, throughput degradation, etc. Forward products are delivered weekly, and are usually reliable. However, operational events, such as decon cycles, extended non-operational (no-op) periods (See Section Appendix A.5.1), and commanded thermal adjustments can push the instrument outside of the training range used to derive the calibration coefficients, introducing errors. The retrospective stream uses interpolated calibration coefficients based on calibration measurements that span the period covered by the observations, and therefore better represent the actual instrument conditions. The retrospective stream is generally considered to be more reliable than the forward stream and is recommended for science applications that require the highest accuracy. Additional details on the OCO-3 data flow can be found in Appendix A.4.

2.2. Observation modes

OCO-3 has four science observation modes; nadir (ND), glint (GL), target (TG), and snapshot area mapping (SAM) mode. The ND and GL observation modes are very similar to those used by OCO-2, except that the agile pointing system allows rapid movement between modes, so GL data is collected over all large water bodies, and ND over nearly all land (excluding, for example, small islands). Nadir-land (NL) and glint-water (GW) viewing are the primary focus of this paper, with detailed discussion of the vEarly data given in Sections 4 through 6.

OCO-3 operates primarily in either ND or GL, but sequences are generated for TGs and SAMs on an orbit-by-orbit basis. To facilitate scheduling of science observations, along with OCO-3 calibration activities, the OCO-3 project uses the JPL-developed "Compressed Large-scale Activity Scheduling and Planning" (CLASP) software. A table of TG and SAM site priorities is maintained by the OCO-3 team. Based on the ephemeris data and geometric/viewing restrictions, the CLASP software determines which targets in the table might be visible for each orbit, applies the priorities to de-conflict any periods when multiple sites are visible, and adds the selected TGs and SAMs to the command sequence. CLASP is also used for ND and GL planning. Additional details can be found in Appendix A.2.

To record a SAM, the OCO-3 PMA is commanded to collect (nearly) adjacent swaths of data to create a small map spanning approximately 80×80 km over a $\simeq 2$ min period. SAM sites include volcanoes, ecological and agricultural field stations, power plants and fossil fuel

emission hot-spots, allowing for a variety of carbon cycle science questions to be explored. In early operations, the priority list contained approximately 90 volcanoes, 20 Total Carbon Column Observing Network (TCCON) validation sites (Wunch et al., 2011), 4 Collaborative Carbon Column Observing Network (COCCON) validation sites (Frey et al., 2019), 14 SIF tower sites (Yang et al., 2018), 200 cities and power plants, and 80 sites coordinated with the NASA ECOsystem Spaceborne Thermal Radiometer Experiment on Space Station (ECOSTRESS) (Fisher et al., 2020). Specific field sites can be added temporarily for co-ordinated campaigns. To aid in early operations investigations, 10 flat desert sites, which have little topography and no expected variation in XCO$_2$, were also selected. SAMs are discussed in more detail in a forthcoming paper.

The TG mode collections are similar to those from OCO-2, and provide the primary source of data for validating the XCO$_2$ estimates retrieved from OCO-3 observations (Wunch et al., 2017). However, there are two substantial differences between OCO-2 and OCO-3 TG observations. First, rather than dithering the satellite bus so that the instrument takes many hundreds of overlapping soundings spanning only a few tens of kilometers parallel to the orbit track, OCO-3 collects a series of relatively long segments (usually 5 or 6) with the PMA locked during each one. This creates a sequence of overlapping swaths that extend parallel to the orbit track. The second difference is that since the PMA is locked within each segment, the OCO-3 TG collection will contain only a single observation geometry per segment, in contrast to OCO-2 which continuously varies the observation geometry during the TG collection. In addition, the more modern flight computer in OCO-3 allows a very large list of TG sites to be maintained. This is in contrast to OCO-2, where the TG list is limited to 28 sites in 2020, an increase from 19 at launch, the coordinates of which have to be uploaded to the on-board software.

Although TG and SAM observations make up only about 2% of the total data volume, these data are of critical importance for both the calibration and validation of OCO-3. They are also expected to yield new insights into the carbon cycle at regional scales. Hundreds of TG and SAM observations were successfully collected during the first few months of operations. While there are some residual pointing issues (see Section 2.1.3), these measurements clearly demonstrate the value of these observing modes.

2.3. Science planning

The planning of data collection is organized by the mission operations team as discussed in detail in Appendix A. The science observations are planned for periods with adequate sunlight, while calibration measurements are taken during solar eclipse. Science data collection are sometimes interrupted by the Mission Operations System (MOS) for planned ISS station activities and instrument decontamination cycles, or unplanned instrument safing events. In addition, unplanned outages of the Huntsville Operations Support Center (HOSC) data flow occur.

OCO-3 is required to collect science data during at least 50% of the orbits not impacted by ISS or HOSC related outages. Table 3 shows that data were collected $\simeq 80\%$ of observable orbits between 6 August 2019 and 31 March 2020. The only months that fell below the requirement were October, due to GPS outages, sequence aborts, and the FSW v4.2 update, and November, due to PMACal and instrument decon. Additional details of outages are given in Table A1.

3. OCO-3 sounding selection and preprocessors

Instruments such as OCO-2 and OCO-3 acquire many thousands of soundings each day that must be processed through a chain of computationally expensive algorithms to estimate XCO$_2$. Accurate retrieval of XCO$_2$ is precluded when the scene is contaminated with too much cloud or aerosol (Butz et al., 2009; Aben et al., 2007; O'Dell et al., 2012). It is thereby desirable to prescreen soundings in order to retain

Table 3

Monthly statistics of the OCO-3 collection for the period August 2019 through March 2020.

Month	Total	Orbits containing	Number of	Orbits containing	Number of
	Number of Orbits	HOSC interrupts (% of total)	Observable Orbits (% of total)	MOS interrupts (% of observable)	Collected Orbits (% of observable)
Aug (2019) (beginning on 6th)	355	94 (26.5%)	261 (73.5%)	27 (10.3%)	234 (89.7%)
Sep (2019) (complete month)	465	34 (7.3%)	431 (92.7%)	36 (8.4%)	395 (91.6%)
Oct (2019) (complete month)	481	176 (36.6%)	305 (63.4%)	126 (41.3%)	179 (58.7%)
Nov (2019) (complete month)	465	40 (8.6%)	425 (91.4%)	382 (89.9%)	43 (10.1%)
Dec (2019) (complete month)	482	92 (19.1%)	390 (80.9%)	0 (0.0%)	390 (100.0%)
Jan (2020) (complete month)	480	90 (18.8%)	390 (81.2%)	16 (4.1%)	374 (95.9%)
Feb (2020) (complete month)	449	74 (16.5%)	375 (83.5%)	21 (5.6%)	354 (94.4%)
Mar (2020) (complete month)	480	34 (7.1%)	446 (92.9%)	6 (1.3%)	440 (98.7%)
Grand Total	3657	634 (17.5%)	3023 (82.5%)	614 (20.1%)	2409 (79.9%)

those most likely to yield good quality retrievals of XCO_2. This section describes preprocessor algorithms used for selecting OCO-3 soundings.

3.1. L2FP sounding selection

To reduce the computational expense of running the L2FP algorithm (Boesch et al., 2019) for XCO_2, only a fraction of the soundings that pass the preprocessors and basic checks on the L1b results are selected for processing (Mandrake et al., 2013). Typically 5–20% of the total soundings are selected for the forward stream processing. In the retrospective stream, and during full reprocessing campaigns, the throughput is not limited, such that all of soundings that pass the basic quality checks and cloud flags are processed through L2FP. The sounding selection criteria for OCO-2/3 are given in Table 4. In addition to the stated variables, all soundings are checked for L1b sounding quality flags and preprocessor skip flags.

For the OCO-3 developmental vEarly data set used in this analysis, the sounding fraction was set to 20% for August through mid-October. This provided enough data to determine the L2FP quality flags and bias correction that are discussed in Section 6.2. For the other months in the developmental vEarly data set presented here, i.e., second half of October 2019 through March 2020, only 5% of the soundings were processed through L2FP. However, the vEarly retrospective data being delivered to the NASA DISC will include 100% of the soundings that pass the prescreeners. The OCO-2 v9 data used for comparisons with the OCO-3 results in this manuscript include 100% of the cloud-screened soundings, or $\simeq$ 25% of all soundings collected. These screening differences introduce artificial discrepancies in data volumes that are explicitly noted where appropriate.

3.2. ABP and IDP performance

Early in the OCO-3 mission, the b10 version of the A-Band Preprocessor (ABP) (Taylor et al., 2016) was deployed for both OCO-2 and OCO-3. The main new feature of the ABP code is the addition of a zero level offset to the calculated top of the atmosphere radiances to account for uncalibrated instrument stray light and SIF. ABP b10 also

Table 4

Sounding selection criteria for OCO-2 and OCO-3. Soundings are categorized as either land (land fraction $\geq$ 80%), water (land fraction $\leq$ 20%), or indeterminate (20% < land fraction < 80%).

	NL	GW	TG
Solar zenith	$\leq$ 85	$\leq$ 80	$\leq$ 85
Observation zenith	N/A	N/A	< 50
ABP cloud flag	= 0	= 0	= 0
IDP CO_2 ratio (OCO-2 only)	[0.985, 1.045]	[0.985, 1.045]	N/A
L1b ABO2 SNR	> 100	> 100	N/A
L1b SCO2 SNR	> 75	> 75	N/A

uses gas absorption cross-section tables (ABSCO) v5.1, consistent with those used by the b10 L2FP (Boesch et al., 2019). The IMAP-DOAS Preprocessor (IDP) code (see Section 2.2 of (Taylor et al., 2016)) is essentially unchanged for the b10 software build.

For each observing mode, the b10 ABP was tuned using OCO-2 data to specify the clear-sky surface pressure offsets and retrieved χ^2 threshold parameters (See section 2.4 of (O'Dell et al., 2014)). Because the surface pressure offset is intended to address deficiencies in the ABSCO tables or algorithm physics rather than instrument performance or calibration issues, we assume that tuning adopted for OCO-2 will work well for OCO-3. That appears to be the case since the b10 cloud screening is performing well on early OCO-3 data.

Histograms of differences between the a priori and retrieved surface pressure (ABP variable, dpcld) for OCO-3 versus OCO-2 are shown in the top row of Fig. 4. The middle row shows histograms of the ratios of the CO_2 column abundances retrieved independently by the IDP in the WCO2 and SCO2 channels (IDP CO_2 ratio). The bottom row shows histograms of the ratios of the water vapor column abundances retrieved independently by the IDP in the WCO2 and SCO2 channels (IDP H_2O ratio). CO_2 or H_2O ratios that differ substantially from unity indicate the presence of optically-thick low clouds (Taylor et al., 2016). The H_2O ratio is not used for sounding selection, but is an important part of the L2FP quality filtering described in Section 6.

The left panel of Fig. 5 shows the map of the fraction of soundings passing the ABP cloud flag in each 2° × 2° bin for August (2019) through March (2020). The spatial pattern looks as expected, with high throughput ($\simeq$ 75%) over arid land regions as well as some areas of the subtropical Pacific and Atlantic oceans, and yields of $\simeq$ 15% at the higher latitudes, which tend to be cloudier. The right panel shows the results when the IDP CO_2 ratio filter is included. The largest effects are seen over the tropical forests, specifically the Amazon, Congo and Indonesia, where yields of cloud free scenes are reduced to < 10%.

3.3. OCO-3 validation against GOES ABI

To verify the OCO-3 cloud screening results, we performed a direct comparison to the cloud mask from the Advanced Baseline Imager aboard the Geostationary Operational Environmental Satellite-16 (GOES-ABI) (Schmit et al., 2017). The spectral bands used to create the ABI cloud mask are similar to those used by MODIS, and the ABI cloud mask product has been validated against the MODIS Cloud Mask product (MOD35/MYD35) (Heidinger et al., 2016). Previous research (Taylor et al., 2016) found $\simeq$ 85 ± 3% agreement between OCO-2 cloud screening and the Aqua-MODIS cloudmask for a range of seasons and viewing modes. Here, we hypothesized that the agreement between OCO-3 cloud screening and ABI cloud mask should be similar to the (Taylor et al., 2016) results, given the similarities of the OCO-2 and OCO-3 sensors.

The sounding-by-sounding comparison of cloud masks are quantified by classifying individual scenes into one of four categories;
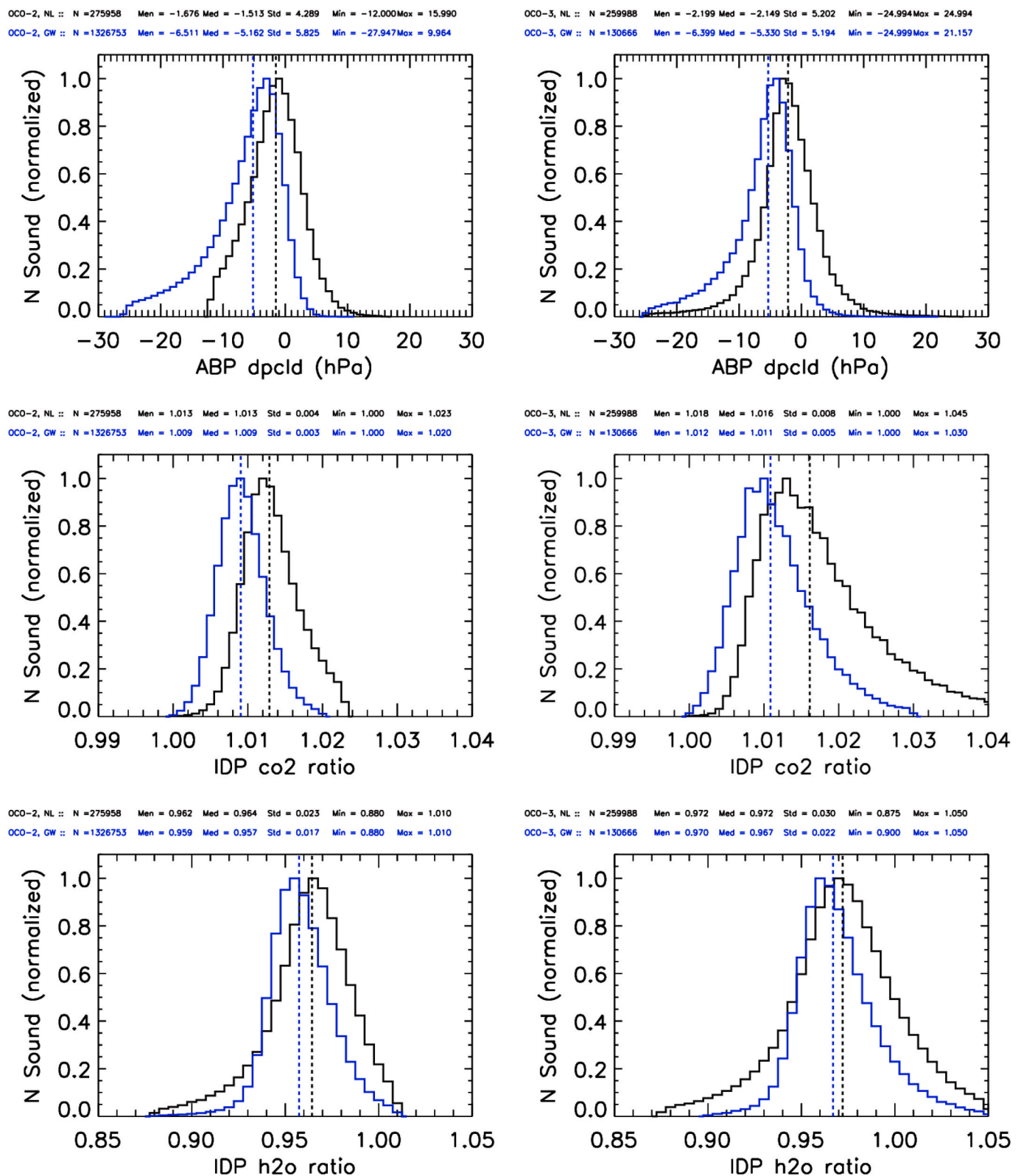
Fig. 4. Histograms of the preprocessor cloud screening variables for OCO-2 (left) and OCO-3 (right). Black and blue curves represent NL and GW soundings, respectively. Top row shows ABP dpcld, middle row shows IDP CO_2 ratio, and lower row shows IDP H_2O ratio. Median values are given as vertical dashed lines in the respective colors. (For interpretation of the references to colour in this figure legend, the reader is referred to the web version of this article.)

1. OCO-3 clear, ABI clear (True Positive)
2. OCO-3 cloudy, ABI cloudy (True Negative)
3. OCO-3 clear, ABI cloudy (False Positive)
4. OCO-3 cloudy, ABI clear (False Negative)

Three useful statistics are calculated from the categorized results;

1. Throughput; the fraction of scenes that are identified as clear by OCO-3.
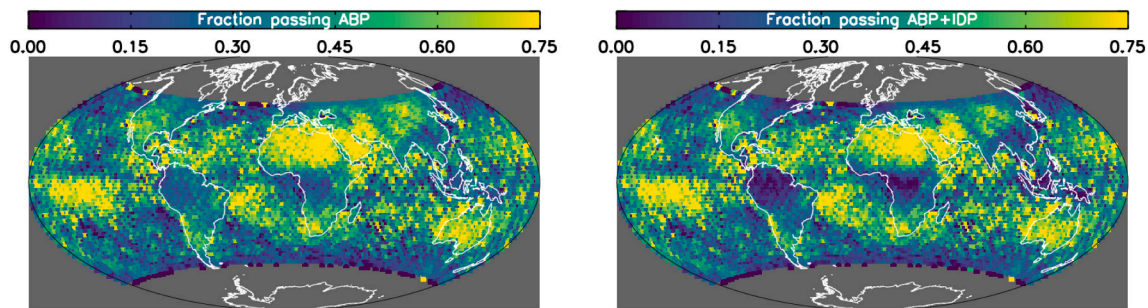
Fig. 5. Fraction of soundings passing the ABP cloud flag (left) and the combined ABP + IDP screening (right) in each 2° by 2° bin for August 2019 through March 2020.

Table 5
Comparison of the OCO-3 cloud screening preprocessors to GOES ABI cloud mask. Results are shown for NL and GW viewing for seven select days ranging from 21 December 2019 to 06 January 2020.

Viewing	Reference clear atmospheres					Reference cloudy atmospheres					Throughput	Agreement	Positive predictive value
	Total cases	Predicted clear		Predicted cloudy		Total cases	Predicted clear		Predicted cloudy				
		N_{TP}	TPR	N_{FN}	FNR		N_{FP}	FPR	N_{TN}	TNR			
ABP-only													
Nadir-land	117,394	78,987	67.3%	38,407	32.7%	163,716	13,617	8.3%	150,099	91.7%	32.9%	81.5%	85.3%
Glint-water	215,089	177,207	82.4%	37,882	17.6%	274,152	30,922	11.3%	243,230	88.7%	42.5%	85.9%	85.1%
ABP + IDP													
Nadir-land	117,394	55,582	47.3%	61,812	52.7%	163,716	3970	2.4%	159,746	97.6%	21.2%	76.6%	93.3%
Glint-water	215,089	175,645	81.7%	39,444	18.3%	274,152	28,530	10.4%	245,622	89.6%	41.7%	86.1%	86.0%

2. Agreement; the fraction of scenes that are correctly classified by OCO-3 relative to the ABI reference state.
3. Positive predictive value; the fraction of the ABI clear soundings also predicted clear by OCO-3.

Table 5 summarizes the results for 7 days (38 granules) in December 2019 and January 2020 in both NL and GW viewing modes. Results are shown when only the ABP cloud flag is used and when the IDP CO_2 ratio is added. The reference ABI cloud mask remains the same in each case. The results are comparable to those shown in Table 2 of (Taylor et al., 2016). Specifically, the agreement ranges from a low of 77% for NL to a high of 86% for GW when the ABP is combined with the IDP. In addition, the throughput decreases and the positive predictive value increases, as expected, for the ABP + IDP combination. In summary, these cloud screening verification results are consistent with expectations, indicating acceptable performance of the OCO-3 cloud screening for vEarly data release.

4. Data sampling and L1b characteristics

This section explores the spatial and temporal sampling and the L1b characteristics of the OCO-3 vEarly data. Comparisons are made to the OCO-2 v8 product (OCO-2 Science Team et al., 2017a), as these are the latest L1b available at the time since the v9 reprocessing did not contain updated L1b (see discussion in Section 6.1). After providing an analysis of monthly observation mode statistics in Section 4.1, the spatial sampling in the NL and GW observation modes is analyzed in Section 4.2. A discussion comparing and contrasting the polarization sensitivity of OCO-2 and OCO-3 is provided in Section 4.3, while Section 4.4 highlights differences that drive expected signal to noise ratios of the two instruments.

4.1. Observation mode statistics

Table 6 compares observing mode statistics month by month for OCO-2 and OCO-3 for August 2019 through March 2020, revealing several differences in the two data sets. First, although the two sensors collect data at exactly the same frequency (3 Hz) and with the same number of footprints per frame (8), the collection volume of OCO-3 is only ≃60% that of OCO-2 during this 8 month time period. The discrepancy in volume reflects differences in operating aboard the ISS (OCO-3), where operations are often interrupted as noted in Section 2.3 and Appendix A, versus operating with a dedicated satellite bus (OCO-2). Recalculating the summary statistics excluding August (which was only a partial month for OCO-3), October (which had a number of OCO-3 MOS interrupts), and November (which included OCO-3 PMAcal), yields an OCO-3 collection volume ≃ 80% the size of the OCO-2 volume. As the daily operations of OCO-3 pointing and control mature, higher acquisition rates are anticipated. However, there will continue to be interruptions outside the control of the OCO-3 project that will result in loss of science data.

Another significant difference between the two datasets is that a large fraction (≃ 73%) of the OCO-3 data was collected in nadir viewing mode (NL + NW) during the first 8 months of operation, compared to only ≃ 33% for OCO-2. Although the NL data is highly useful, the NW observations cannot be used to retrieve XCO_2 due to extremely low SNR. During some periods, the large fraction of OCO-3 NW observations was due to PMA control issues precluding glint, TG or SAM observations for extended periods (see Table A2). However, there are sometimes physical viewing constraints on glint observations due to high solar beta angles (see Section 4.3) and/or ISS obstructions (see Appendix A.2), requiring nadir-only viewing.

Table 6 also reveals a substantial difference in the volumes of glint observations due to the aforementioned issues. Nearly half of all the OCO-2 data collected over the 8 month period were GW, while for OCO-3 only ≃ 20% were GW observations. The flexibility of the PMA enables OCO-3 to change viewing modes multiple times within a single orbit, unlike OCO-2 which operates in a single viewing mode per orbit (with the exception of TG mode viewing). Therefore, many less glint-land (GL) observations are made by OCO-3 (≃ 0.3% averaged over 8 months) compared to OCO-2 (≃ 19% averaged over 8 months). The GL data can be used by flux inversion modelers to estimate CO_2 sources and sinks

Table 6
Monthly observation mode statistics comparing OCO-2 to OCO-3 for the time period August 2019 through March 2020.

		NL	NW	GL	GW	TG	SAM	XS	Total
201908	OCO-2	420 (11%)	816 (22%)	540 (14%)	1891 (51%)	6.3 (0.2%)	–	18.0 (0.5%)	3744
	OCO-3	769 (37%)	904 (43%)	7 (0%)	335 (16%)	1.1 (0.1%)	3.5 (0.2%)	55.1 (2.6%)	2096
201909	OCO-2	440 (12%)	765 (21%)	570 (16%)	1819 (50%)	8.6 (0.2%)	–	21.6 (0.6%)	3673
	OCO-3	501 (16%)	2262 (73%)	3 (0%)	218 (7%)	3.0 (0.1%)	19.2 (0.6%)	56.4 (1.8%)	3083
201910	OCO-2	510 (13%)	748 (20%)	732 (19%)	1761 (46%)	7.3 (0.2%)	–	17.6 (0.5%)	3817
	OCO-3	454 (33%)	648 (47%)	3 (0%)	144 (11%)	7.0 (0.5%)	46.4 (3.4%)	45.6 (3.3%)	1375
201911	OCO-2	531 (14%)	716 (19%)	787 (21%)	1653 (44%)	5.3 (0.1%)	–	13.7 (0.4%)	3732
	OCO-3	34 (14%)	85 (34%)	0 (0%)	111 (44%)	0.8 (0.3%)	2.5 (1.0%)	12.8 (5.1%)	251
201912	OCO-2	540 (14%)	718 (19%)	830 (22%)	1691 (44%)	6.0 (0.2%)	–	14.0 (0.4%)	3820
	OCO-3	660 (26%)	1455 (58%)	5 (0%)	280 (11%)	2.6 (0.1%)	10.1 (0.4%)	70.5 (2.8%)	2509
202001	OCO-2	441 (14%)	564 (18%)	661 (21%)	1415 (45%)	5.1 (0.2%)	–	13.2 (0.4%)	3119
	OCO-3	353 (13%)	1411 (52%)	5 (0%)	727 (27%)	6.3 (0.2%)	15.6 (0.6%)	170.5 (6.3%)	2705
202002	OCO-2	497 (14%)	685 (19%)	715 (20%)	1633 (45%)	9.3 (0.3%)	–	24.7 (0.7%)	3600
	OCO-3	770 (31%)	905 (37%)	11 (0%)	589 (24%)	9.9 (0.4%)	39.2 (1.6%)	104.6 (4.3%)	2460
202003	OCO-2	467 (12%)	770 (20%)	636 (17%)	1844 (48%)	11.2 (0.3%)	–	30.6 (0.8%)	3808
	OCO-3	575 (16%)	2033 (58%)	9 (0%)	716 (20%)	8.5 (0.2%)	46.6 (1.3%)	99.7 (2.8%)	3522
Mean	OCO-2	481 (13%)	723 (20%)	684 (19%)	1713 (47%)	7.4 (0.2%)	–	19.2 (0.5%)	3664
	OCO-3	515 (23%)	1213 (50%)	5 (0%)	390 (20%)	4.9 (0.2%)	22.9 (1.1%)	76.9 (3.6%)	2250

Reported values are the number of measurement frames (8 footprints per frame), in thousands. Percentages of the monthly total are shown in parenthesis for each mode.
Total number of soundings (OCO-2) = 29,316.
Total number of soundings (OCO-3) = 18,007.

(Crowell et al., 2019), but offer no advantages over NL data.

The fraction of TG mode data collected was $\simeq 0.2\%$ of the total data volume for both sensors. These data are essential for vicarious calibration and XCO_2 validation, as will be discussed in Section 6. OCO-3 SAM mode data comprise $\simeq 1\%$ of the total data volume. The fraction of transition data (XS), observations collected while the OCO-2 or OCO-3 instrument is transitioning between observation modes or while the PMA is in motion, is much higher for OCO-3 (3.6% averaged over 8 months) than OCO-2 (0.5%) due to the higher frequency of mode switching for OCO-3. The XS data contain unknown, but likely little, science value.

Fig. 6 shows bar charts of the monthly observation mode statistics for OCO-2 (top) and OCO-3 (bottom). For OCO-2, the monthly volume is stable at $\simeq 3600$ k soundings, with approximately 50% being taken in GW mode, and the other 50% being evenly distributed between NW, GL and NL modes. For OCO-3, the monthly data volumes have varied significantly due to the no-ops periods and the large loss of OCO-3 science data in November during PMACal. This figure highlights the large fraction of NW data that has been collected thus far by OCO-3. The expectations are high that this portion of the data will decrease as the project matures.

4.2. Temporal and spatial sampling of NL and GW observations

This section shows sampling patterns of the nominal nadir-land and glint-water collected from August 2019 through March 2020 for OCO-3 and August 2019 through January 2020 for OCO-2. Unfortunately, at end of January 2020 the OCO-2 project began generating the v10 products and the v9 Lite files were not available for February and March. Only results for footprint 4 out of the eight returned for each measurement frame are shown. For this analysis, the other footprints were found to produce statistically indistinguishable results.

The spatial and temporal sampling of the OCO-2 and OCO-3 datasets differ due to the ISS and OCO-2 orbits covering different latitudes and different times of day. As noted above, OCO-2 has a near-polar, sun-synchronous orbit with a 1:36 PM ascending equator crossing time on the illuminated hemisphere. The ISS orbit does not repeat exactly, but has an approximate orbit repeat every 3 days, and a 63-day cycle when it returns to very similar illumination conditions. Fig. 7 shows maps of both the acquisition time of day, given in hours from local noon (HFLN) (top row) and the solar zenith angles (bottom row) for OCO-2

(left) versus OCO-3 (right). The data are displayed on a sounding-by-sounding basis in these plots, highlighting the differences in the spatial sampling patterns of the two sensors.

The OCO-2 sampling pattern is relatively simple, with a smooth time gradient across every orbit. The daylight ascending nodes begin at approximately $+2.5$ HFLN at the southern terminus, have an equator crossing time of $\simeq +1.5$ HFLN (1:30 PM), and a northern terminus at $\simeq +0.5$ HFLN. In contrast, the OCO-3 data span a range of ± 6 h from local noon, with both daylight ascending and descending nodes as the ISS orbit precesses through its 63-day illumination repeat cycle. This diurnal sampling will facilitate addressing a range of carbon cycle science questions that require dawn to dusk coverage. These differences are also relevant to the data quality, since the illumination conditions (solar zenith angle) affects the measurement signal-to-noise ratio (SNR).

Another factor that affects the sampling is the day-to-day on-board operations of the ISS. As was discussed in Section 2.3 and Appendix A, during the first months of OCO-3 operations, there were a number of significant no-op periods in which no science data was collected. In contrast, the more mature OCO-2 had nearly flawless operation during this particular time period. These operational outages are clearly seen in Fig. 8, which shows the relationship between measurement time (days since 1 Aug 2019), HFLN, and latitude for OCO-2 (left) and OCO-3 (right). Notice the OCO-3 data outage in November ($\simeq$ days 85–115) due to PMACal. For OCO-3, the precessing orbit causes a sinusoidal pattern in the HFLN and latitude as a function of time. The difference in the latitudinal extent of the two sensors is evident in these plots, with OCO-2 ranging from $\simeq 65°$ N ($\simeq 75°$ S) in the northern (southern) hemisphere summer. The range of the OCO-3 measurements is $\simeq 52°$ N to $\simeq 52°$ S, in a sinusoidal pattern, as dictated by the precessing orbit of the ISS.

The upper set of panels in Fig. 9 compare the gridded sounding densities of OCO-2 and OCO-3 since 1 August 2019. There are two discrepancies in this comparison worth noting. First, the time span of the OCO-2 data is 6 months, compared to 8 months for OCO-3. Second, 100% of the OCO-2 v9 data that passed the screening algorithms was processed through L2FP. Due to these differences, the OCO-2 data are plotted using a much higher range (1–500) compared to OCO-3 (1–100).

As noted above, the collection rate of GW for OCO-3 was very low in 2019 as the team addressed PMA pointing issues. This is evident in the
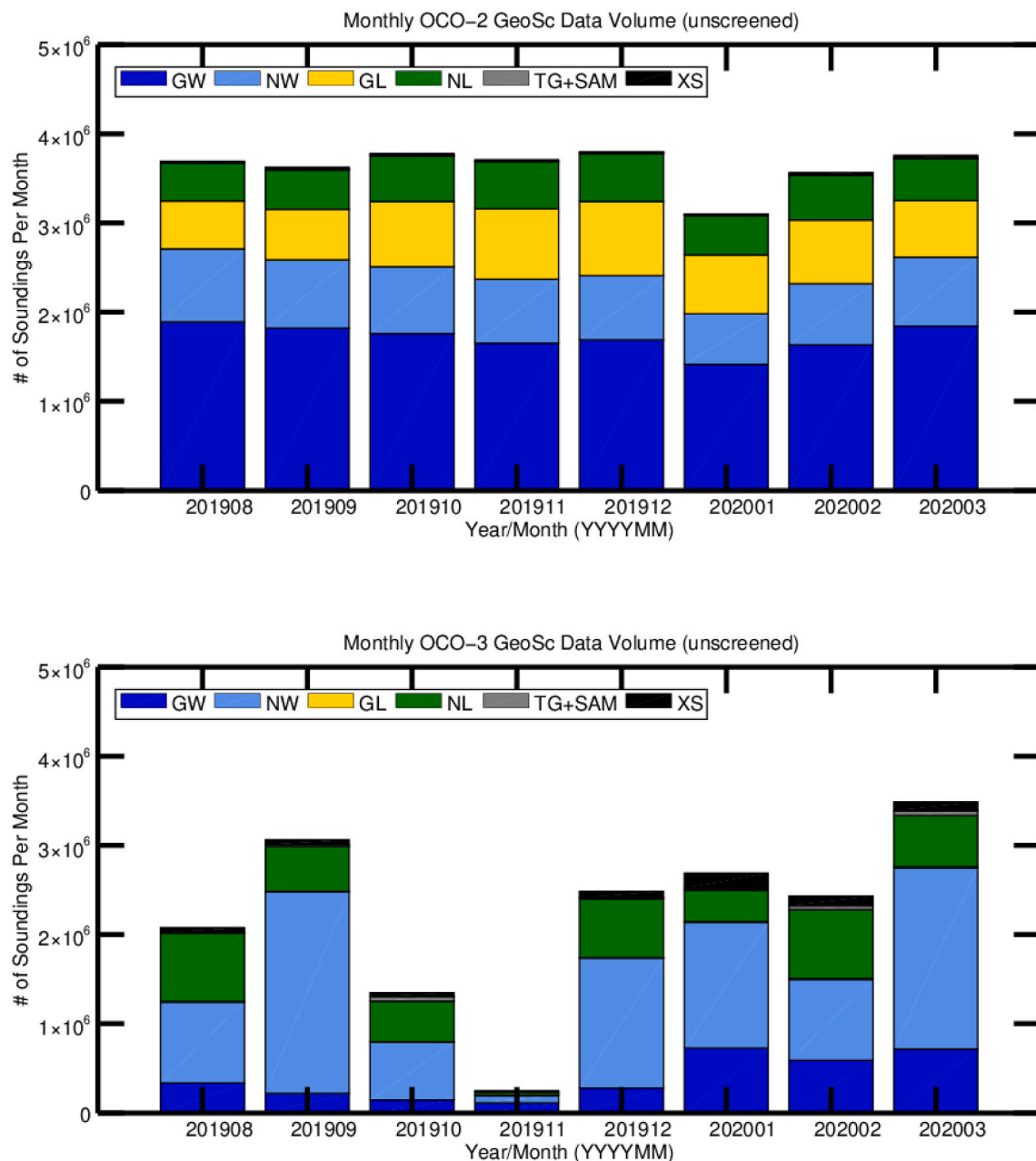
Fig. 6. Monthly data volume by observation mode for OCO-2 (top) versus OCO-3 (bottom) from August 2019 through March 2020.

maps as modest count rates over the oceans compared to OCO-2. Early in 2020, the PMA control and sequencing had become reliable enough that the acquisition of GW observations became more routine. During this time period OCO-3 collected a very large fraction of data in ND viewing mode, yielding a relatively higher count over land compared to OCO-2. Also, due to the precessing ISS orbit, with inflection points at $\simeq$ 50° latitude, large volumes of NL are expected.

The two lower sets of panels in Fig. 9 display Hovmöller plots of the sounding densities as a function of day of year for the NL and GW viewing modes separately. Here we again see the OCO-3 data outage (both NL and GW) for November (2019) during PMAcal, as well as the relatively sparse GW sampling during the first 5 months of operation (through 2019). Another significant difference is the high distribution of OCO-3 NL soundings for > 40° latitudes at the ISS orbit inflection, aka turn-around, points. For OCO-3 in 2020, the distribution of NL and GW counts is more even as the pointing control of the PMA improved.

4.3. OCO-3 polarization response

Since OCO-3 contains a linear polarizer (similar to OCO-2), the polarization response is most easily described by a single polarization angle, which contains the angle between the polarization acceptance axis and the observation reference plane (Eldering et al., 2019b). For OCO-2, the spectrometer is fixed to the spacecraft, so the polarization angle can be altered by changing the spacecraft orientation (See section 6.4 of (Crisp et al., 2017)). For OCO-3, the polarization angle is directly related to the orientation of the boresight as viewed through the PMA. During flight, the boresight view rotates whenever the PMA moves in azimuth or elevation, resulting in a complicated variation of polarization angle as the PMA is repositioned to track targets or the solar glint spot. Further information about the PMA polarization response can be found in Section 4.3 of (Osterman et al., 2020).

The PMA polarization was not correctly modeled for the analysis reported in the OCO-3 pre-launch simulation paper (Eldering et al.,
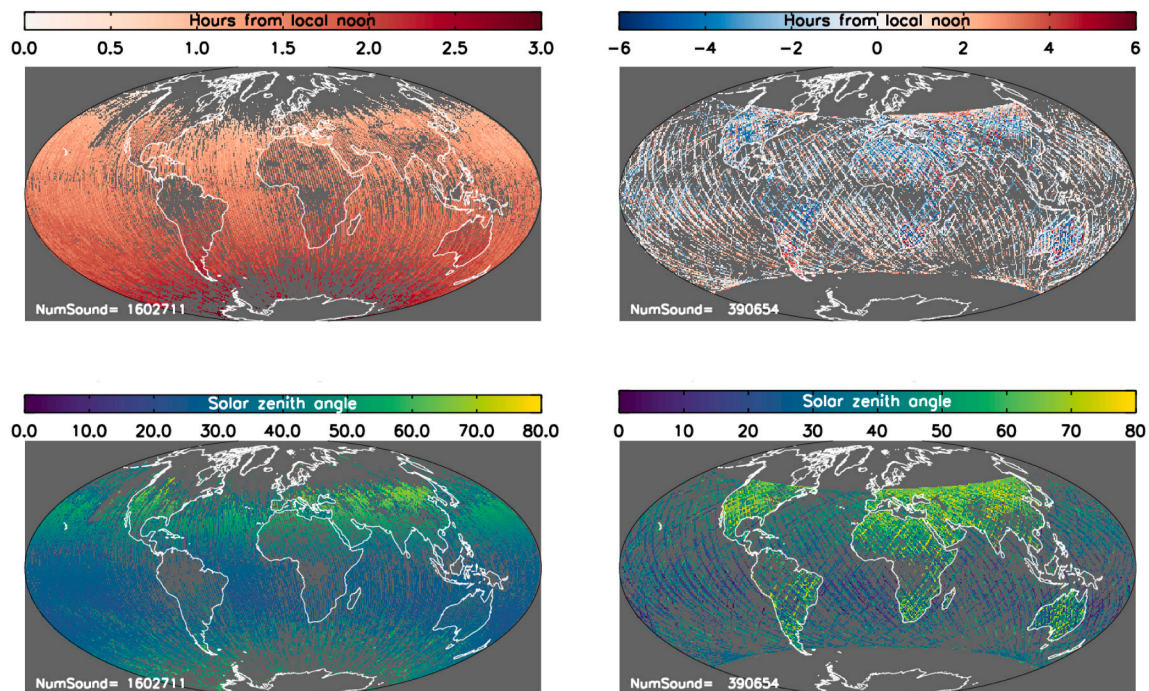
Fig. 7. Sounding-by-sounding hours from local noon (HFLN) (top) and SZA (bottom) maps for OCO-2 (left) and OCO-3 (right). Both the OCO-3 and OCO-2 data have been filtered using their respective quality flags. Note the significant difference in HFLN scales for the two sensors.
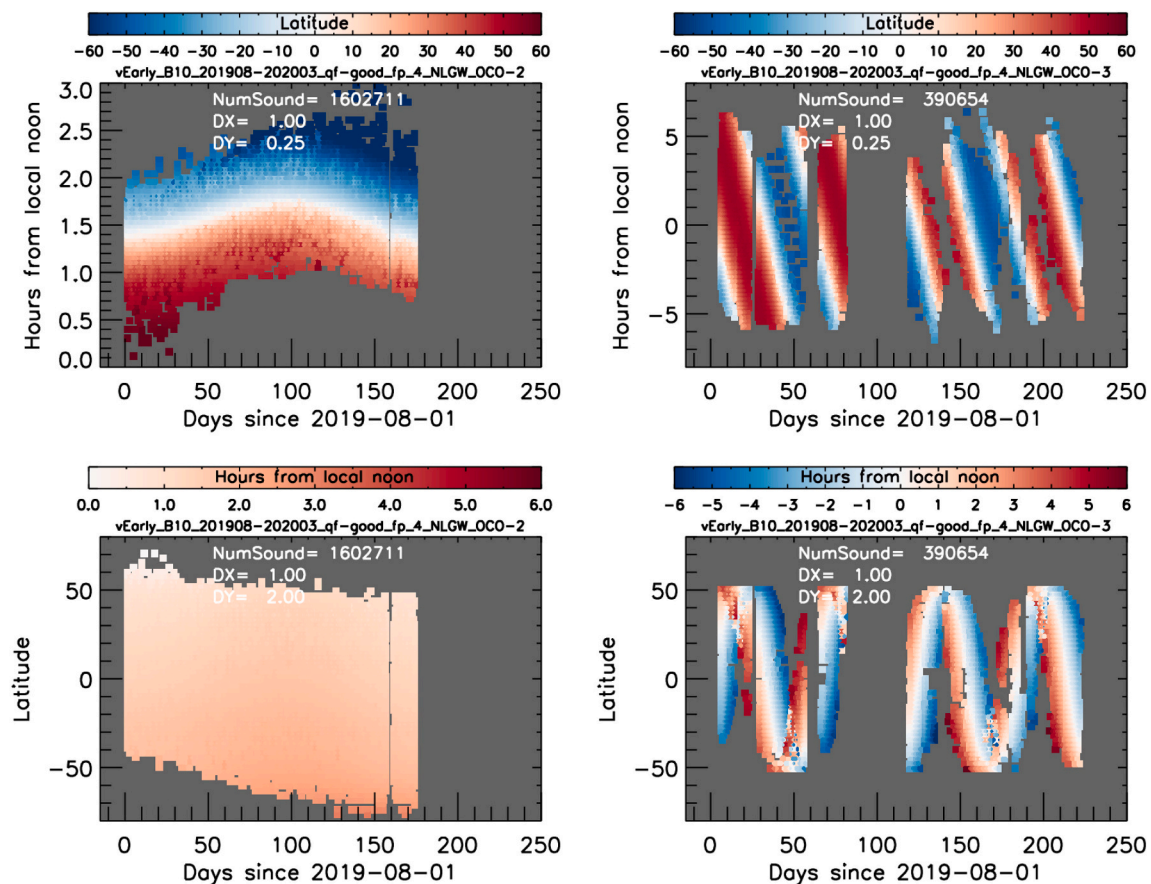

Fig. 8. The relationship between measurement time (days since 1 Aug 2019), hours from local noon (HFLN), and latitude for OCO-2 (left) and OCO-3 (right). The upper panels plot HFLN on the ordinate and latitude in colour, while the lower panels plot latitude on the ordinate and HFLN in colour. Here, the NL and GW data are combined. The OCO-2 data runs through end of January 2020, while the OCO-3 data runs through end of March 2020. Both the OCO-2 and OCO-3 data have been filtered using their respective quality flags.
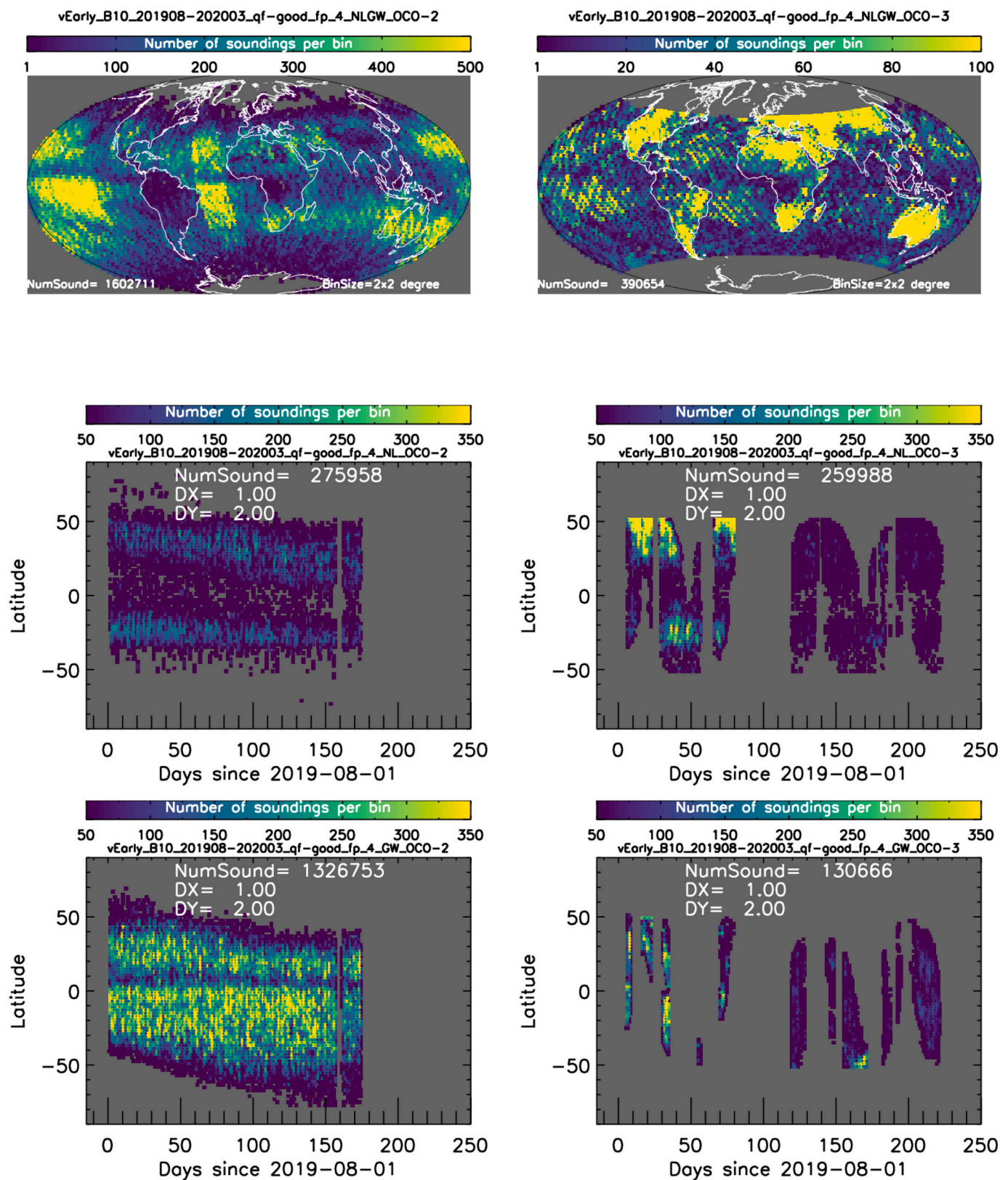
Fig. 9. Sounding densities for OCO-2 (left) and OCO-3 (right) since 1 Aug 2019. The top row shows the maps of sounding densities per 2˚ by 2˚ bin, while Hovmöller plots of the sounding densities are shown for NL (middle row) and GW (bottom row) binned in 1 d by 2˚ latitude increments. Values should be inflated by 8 to obtain the full sounding densities since the data have been filtered to only footprint 4. Both sensors have been screened using their respective L2FP quality filters described in Section 6.
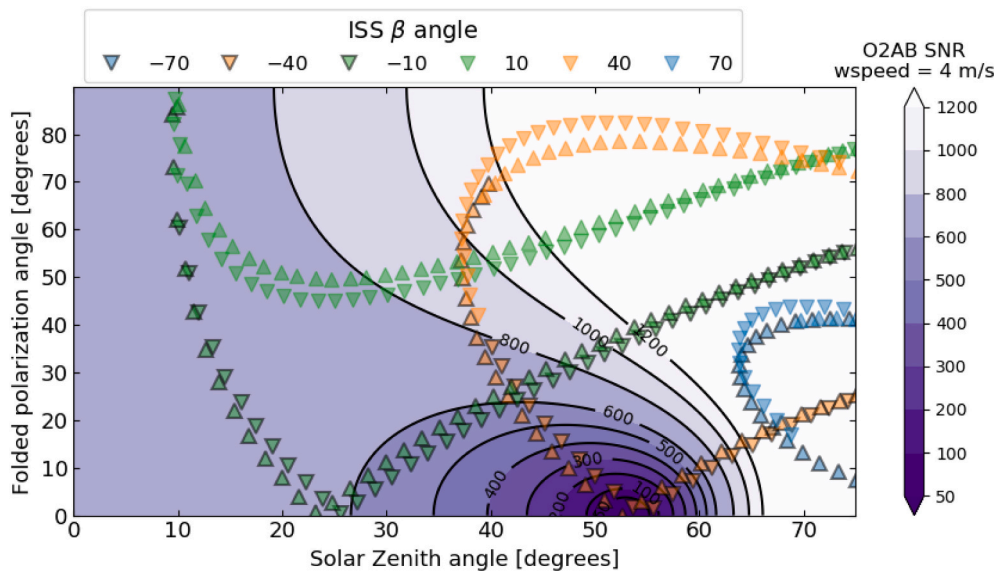
Fig. 10. SNR calculation for Cox-Munk surface model as a function of SZA and polarization angle (background filled contours), with overplotted lines for various paths followed by the PMA for GW observations. The overplotted symbols are colored by the absolute value of ISS β (70 = blue; 40 = green; 10 = orange), with the negative ISS β symbols including a dark gray border. The triangles with a up or down pointing refer to positive or negative PMA elevation angles. (For interpretation of the references to colour in this figure legend, the reader is referred to the web version of this article.)

2019a) due to an incomplete understanding of the variation in the instrument response. Fig. 10 shows a recreation of Fig. 6 from the pre-launch work, but with the addition of example PMA paths during GW observations derived from the set of simulated OCO-3 orbital geometries used in (Eldering et al., 2019a). The primary parameter that controls the paths' location in this parameter space is the ISS β angle, which is the angle between the ISS orbital plane and the vector from Earth to Sun. The original PMA polarization model used in (Eldering et al., 2019a) was close to the correct model for zero ISS β angle, which is the case where the ISS orbit passes directly over the glint spot in the middle of the sunlit portion of the orbit. Each 63 day illumination cycle moves through one cycle in ISS β angle, further modified by a seasonal variation due to Earth's axial tilt. As shown in Fig. 10, when the ISS β angle is −40, the PMA moves through an unfavorable polarization angle very close to the Brewster angle for water, where the reflected light is nearly 100% polarized.

Through an entire 63 day illumination cycle, nearly all polarization angles will be sampled by OCO-3 for GW observations. This implies that some GW observations will be taken with unfavorable polarization angles, when the surface illumination and angles (viewing and solar) are near the Brewster angle (≃ 53°) and have very low SNR. Fig. 10 shows that GW observations collected when the ISS β angle is close to −40° will have low SNR for part of the orbit. There is no mitigation for these low SNR observations (as was done with OCO-2 by rotating the spacecraft about its yaw axis (Crisp et al., 2017)), but in practice this will impact a small amount of the GW data.

Fig. 11 shows latitude-time distributions of observed SNR in the WCO2 spectral band for OCO-3 vEarly clear-sky, quality filtered (see Section Appendix B.2) GW soundings (top), versus two simulated data sets (middle and bottom). Because of the complicated behavior of the polarization angle, individual bins in the latitude–time space will often have bimodel SNR distributions. This typically occurs in cases where the ascending and descending portions of the orbit have very different polarization angles due to the varying orientation of the PMA.

To better understand the occurrence of the low SNR soundings, Fig. 11 displays the smallest decile (the tenth percentile) in SNR for each of the two dimensional histogram bins. The simulated dataset in the middle panel used the sounding geometries and meteorological wind speeds from the observed dataset, but the SNR was recomputed using a simple radiance calculation that assumed no atmospheric scattering or absorption, coupled with a Cox-Munk ocean surface (Cox and Munk, 1954). The correspondence between the two SNR fields gives confidence in the accuracy of the updated instrument polarization

model.

The bottom panel of Fig. 11 shows a similar SNR field computed from the 2015 simulated data used in (Eldering et al., 2019a). In this case, the same simplified Cox-Munk surface model was used, but included a fixed wind speed of 6 m/s. As with OCO-2, GW data is collected with an off-pointing to the true glint spot to avoid measuring extremely high radiances falling outside the calibrated range of the instrument, as would often occur at large SZA (Vincent, 2018). The early mission data used a simple off-pointing strategy, with fixed offset angles (6°, 8°, 10°) for ranges in SZA (0–40°, 40–50°, and 50–60°, respectively). This same off-pointing strategy was also applied to the simulated observations. The ISS β angle does change slightly year to year, but to first order the difference is a small time shift. In this plot, a time shift was applied to the simulated time series to better line up the β angle pattern from 2015 with the observed data covering late 2019 to early 2020. Since it is free of data gaps, the simulated data shows the underlying pattern of low SNR locations and times more clearly, revealing similar patterns of low SNR for the lowest decile compared to the observations.

The early mission off-pointing strategy for OCO-3 was conservative - intended to ensure the radiance limits were not exceeded, with margin in case of pointing errors before the PMA pointing calibration was completed (Section 2.1.2). In addition, the off-pointing values were derived from the pre-launch PMA polarization model. Analysis is currently being done to refine the off-pointing strategy in order to increase SNR and to account for the ISS β angle dependence as well as the SZA. The new off pointing strategy is currently planned to be implemented and tested in late spring or summer of 2020.

4.4. Spectrometer signal to noise

Fig. 12 shows the SNR histograms for each spectral channel (colors) and viewing mode (NL left, GW right) comparing OCO-2 (top) to OCO-3 (bottom), with the vertical bars marking the median SNR for each channel. Both sets of data have been filtered by their respective quality flags, which are discussed in Section 6.2. A statistical summary is presented in Table 7.

Overall, the observed SNRs are in accordance with pre-launch expectations as seen in Fig. 8 of (Eldering et al., 2019a). Detailed comparisons for NL observations are complicated by the differences in the temporal and spatial sampling of the heterogeneous land surfaces. For GW observations, the surface reflectance is more consistent between the two sensors, which results in SNR distributions with similar shapes,
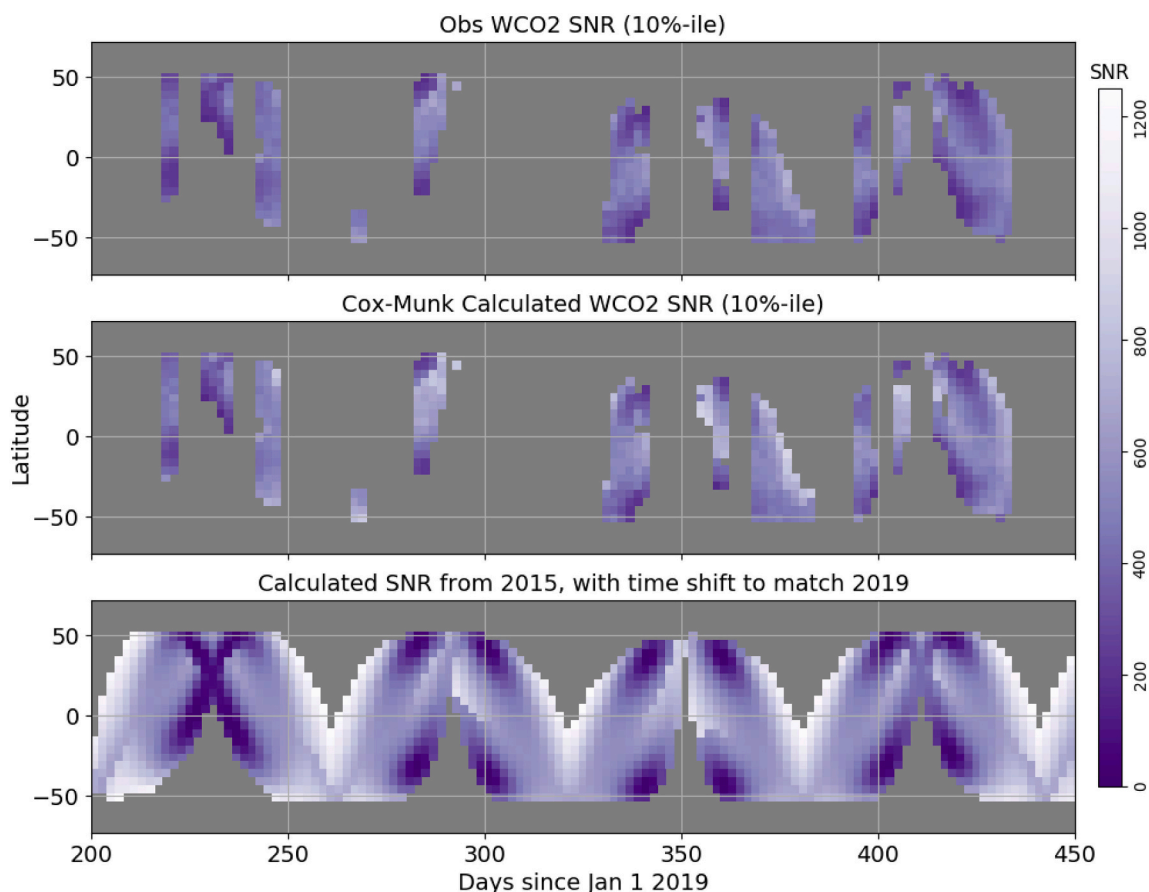
Fig. 11. SNR as a function of time and latitude for OCO-3 vEarly GW soundings. Each panel shows the smallest decile of SNR in each two dimensional histogram bin (2° latitude × 2 days). Top: the observed WCO2 SNR, taken from the measured L1B GW data (with L2FP quality filtering applied - see Section Appendix B.2). Middle: the calculated SNR using the observed sounding geometries and meteorological conditions, a Cox-Munk surface model, and the OCO-3 PMA polarization model. Bottom: the calculated SNR using the simulated geometries and meteorological conditions from 2015 (Eldering et al., 2019a), but with a fixed wind speed of 6 m/s, and with a 16 day time shift so as to approximately match the ISS β angle from 2019.

although the GW distributions tend to be wider in OCO-3 (standard deviation 30–200% larger) compared to OCO-2. The wider tail toward lower SNR for OCO-3 is driven by observations taken with unfavorable polarization angle (see Section 4.3).

Spatial maps of the WCO2 SNR for OCO-2 and OCO-3 are compared in Fig. 13. In this spectral channel, the brightest scenes (SNR > 800) are found over dry land regions for both sensors, with much lower values over forested regions. For OCO-2, with a ≃ 1:30 P.M. overhead crossing time, the SNR is generally correlated to the surface reflectance, while for OCO-3, with varied time-of-day sampling, i.e., varied SZA and polarization sensitivity (See Section 4.3), the spatial pattern of SNR ranges widely. For GW observations, OCO-2 has a small latitudinal gradient, likely driven by the smooth gradient in overpass time (and hence SZA). On the other hand, the pattern for OCO-3 is highly varying with time of day and SZA sampling.

5. OCO-3 SIF

OCO-3 has the same capability for the retrieval of solar-induced fluorescence (SIF) as OCO-2 (Eldering et al., 2017; Sun et al., 2017). Since the instruments have the same spectral resolution and coverage, the retrieved SIF is directly comparable without the need to account for a wavelength correction between the two. The main difference between instruments are the observation modes and the observation times. While OCO-2 operates in both nadir and glint modes, as well as the special target mode over land surfaces, OCO-3 observes land surfaces in either nadir, target or SAM modes, as discussed in Section 2.3.

5.1. General OCO-3 SIF results

The analysis here is of SIF from OCO-3 using measurements spanning 01 August 2019 through 31 January 2020. Fig. 14 shows a global map, aggregated at 2° latitude by 2° longitude, where retrievals in each grid cell have been temporally averaged. Bias-corrected SIF values are shown in units of percentage of the continuum level radiance.

The same type of physical-based retrieval algorithm as outlined in (Frankenberg et al., 2011) has been applied. The retrieval uses two micro-windows in the O_2 A-band near 757 nm (758.24–759.30 nm) and 771 nm (769.67–770.35 nm), in which some isolated solar lines are present. Since the SIF signal from the surface is an additional source of radiation, it leads to a fractional reduction of the solar lines, which then can be used to decouple the SIF radiance signal from surface reflectance. As for OCO-2, the raw retrieved SIF shows unphysical non-zero values over surfaces which do not feature any vegetation (e.g. ice sheets, deserts). This bias is assumed to be a systematic instrumental effect, therefore the same type of radiance-based bias correction is applied. Scenes over bare surfaces are collected on a daily basis, and the retrieved SIF is analyzed as a function of mean radiance in the band. Such correction curves are constructed for each of the eight footprints per measurement frame and for the two retrieval micro-windows separately. An example is shown in Fig. 15. Qualitatively, the shape of the correction curves are similar to OCO-2, i.e. near-linear as a function of continuum level radiance. There is a notable difference in the magnitudes and slopes of the two retrieval windows. The overall footprint spread, slopes and offsets of the calibration curves are significantly
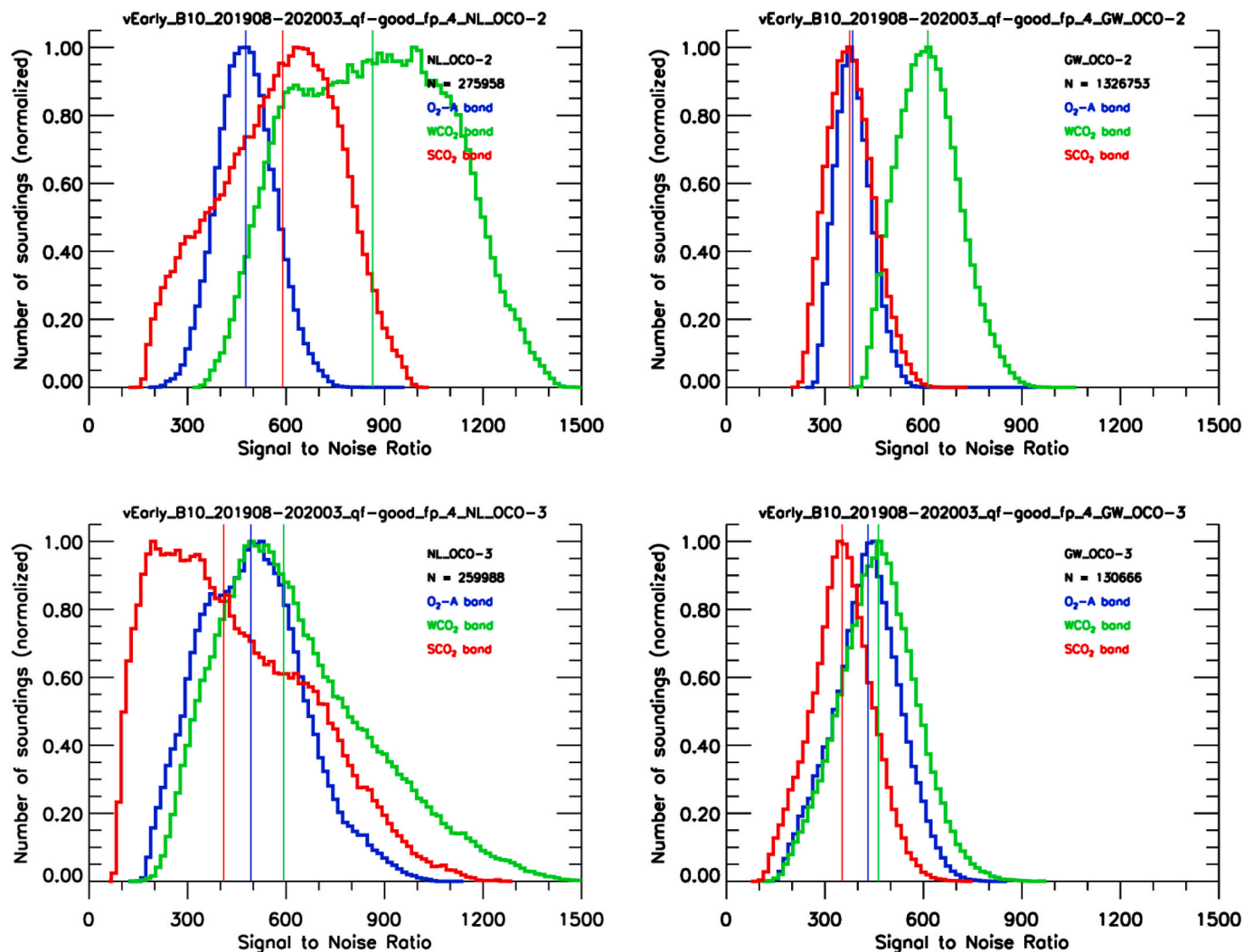
Fig. 12. Histograms comparing the signal to noise ratios for OCO-2 (top) to OCO-3 (bottom) for NL (left) and GW (right). Colors indicate the spectral bands ABO2 (blue), WCO2 (green) and SCO2 (red). Data spans the August 2019 through January 2020 for OCO-2 and August 2019 through March 2020 for OCO-3. Both the OCO-3 and OCO-2 data have been filtered using their respective quality flags. (For interpretation of the references to colour in this figure legend, the reader is referred to the web version of this article.)

Table 7
Signal to noise ratio statistics comparing OCO-3 to OCO-2 for each spectral band (rows) and for nadir-land and glint-water. The median values are given, with the standard deviation in parenthesis.

	OCO-2 NL	OCO-3 NL
ABO2	477 (86)	493 (156)
WCO2	864 (225)	592 (235)
SCO2	590 (177)	410 (230)

	OCO-2 GW	OCO-3 GW
ABO2	384 (53)	431 (102)
WCO2	613 (92)	463 (117)
SCO2	375 (69)	353 (93)

smaller in the 771 nm window. This behavior is most likely caused by the current (vEarly) radiometric calibration.

After removal of the bias, the uncertainty on each retrieved value is ideally only driven by instrument noise. This is evaluated by comparing the reported single-sounding uncertainty, calculated from the posterior covariance matrix, and the true scatter of the retrieved SIF over the Sahara desert. Shown in Fig. 16 (757 nm window only), the true scatter

in the retrieved SIF is 10–20% higher than the reported uncertainty. This points to a systematic under-estimation of the calculated single-sounding uncertainty and is consistent with Fig. 4 from (Sun et al., 2017) which also shows an under-estimation by a similar magnitude in OCO-2 data.

5.2. Comparisons to OCO-2

In this section SIF from OCO-3 vEarly is compared against the v9 operational data stream from OCO-2 (OCO-2 Science Team et al., 2017b) from the same time period. Since both instruments cover the same wavelength ranges in the O_2 A-band, the retrieved SIF can be compared without having to perform a wavelength correction. Since the single-sounding uncertainty on each retrieved scene is the same order of magnitude as the retrieved value itself, data is aggregated over multiple scenes for a robust estimate of the true SIF. A simple aggregate on regular longitude-latitude grid cells is used, with sub-selection for only those days with valid measurements from both OCO-2 and OCO-3. The highly varying overpass times of OCO-3, as well as straightforward sampling biases within a grid cell make the comparison challenging. Therefore, the data for this comparison is further restricted by selecting only those grid cells whose mean continuum level radiance does not
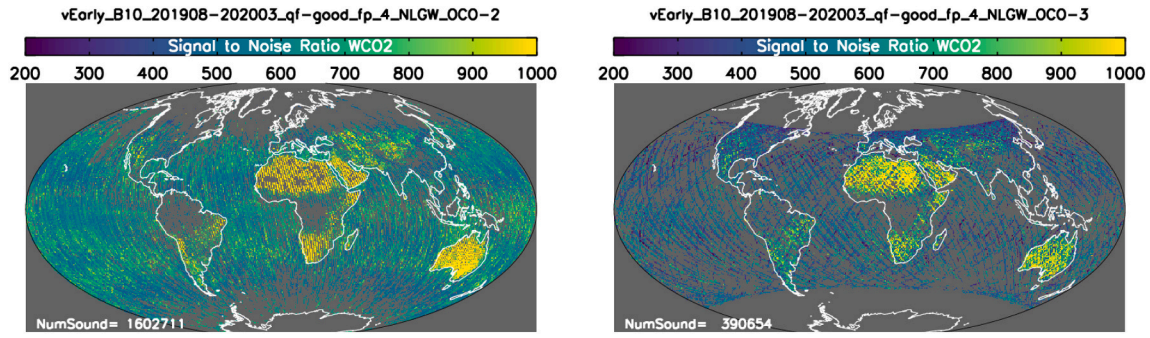
Fig. 13. Single sounding maps of OCO-2 (left) vs OCO-3 (right) signal to noise ratio in the WCO2 spectral band. Data spans August 2019 through January 2020 for OCO-2 and August 2019 through March 2020 for OCO-3. Both data sets have been filtered using their respective quality flags.
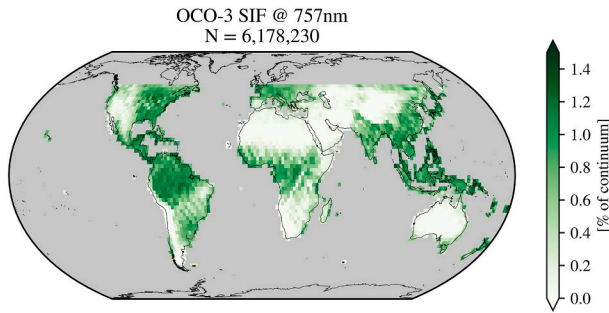

Fig. 14. A global picture of SIF from OCO-3, on a 2° by 2° grid, shows the expected global vegetation pattern for the period 01 August 2019 through 31 January 2020.

differ between OCO-2 and OCO-3 by more than 5 W/m^2/sr/um, the mean reported uncertainty not exceed 0.3 W/m^2/sr/um, and finally every valid grid cell must contain at least 100 successful OCO-2 and OCO-3 retrievals each.

This subset of 293 grid cells is shown in Fig. 17. The comparison is focused on relative SIF only, i.e., the percent relative to the continuum level radiance, as it exhibits much lower dependence on the time of day and the observing geometry. The representation of SIF as a fraction of continuum does not imply a correlation with the continuum itself. It was shown in the past (Plascyk, 1975; Alonso et al., 2008) that this fundamental principle, on which the retrieval algorithm is based, ensures that the retrieved fluorescence contribution to the TOA radiance is decoupled from surface reflectance. The comparison shows a small bias between the two instruments, but the overall agreement in this aggregate comparison is reasonably good with $r = 0.89$.

The ground tracks of OCO-2 and OCO-3 cross several times per day, but at different overpass times. SIF retrievals can be analyzed by finding all ground track crossings which occur over land surfaces, and aggregating subsets of scenes where spatial overlap between OCO-2 and OCO-3 footprints is found. While the majority of track crossings occur over ocean surfaces, a total of 370 groups of scenes were found on the 97 common days on which both OCO-2 and OCO-3 made measurements. Fig. 18 shows the comparisons of the 757 nm SIF of those groups, which have been further sub-selected to only include groups where overpass times differed by less than 15 h. For this comparison, both nadir and glint observation modes are included for OCO-2. There is more scatter and larger bias in the comparison of OCO-3 data against OCO-2 glint compared to OCO-2 nadir, however the data record is too short to make a statement about the SIF emission angle being a contributing factor. The overall correlation between OCO-2 and OCO-3 SIF is better than for the grid-cell comparison with $r = 0.94$ and $r = 0.93$ for OCO-2 nadir and OCO-2 glint, respectively. Note that while there is a geolocation error up to a few kilometers in the vEarly OCO-3 data stream, this analysis removes the main sampling bias compared to grid
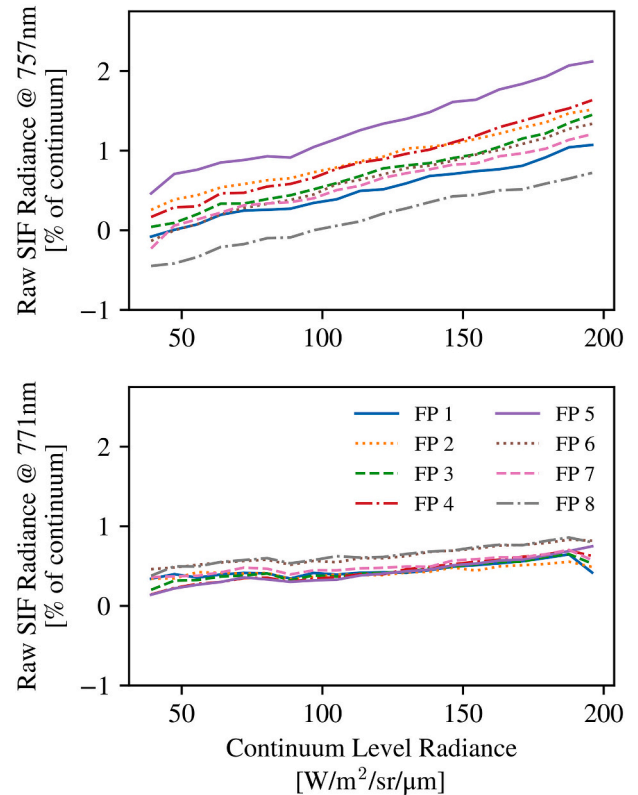

Fig. 15. Correction curves for the 757 nm and 771 nm retrieval windows, constructed from scenes measured in September 2019 over the Sahara desert in which no vegetation and thus no SIF is expected. The retrievals report relative SIF values of −0.5% to 2.0%, rather than the assumed true value of 0%. Using these correction curves, each OCO-3 SIF retrieval receives a bias corrected value dependent on its specific continuum level radiance. The different lines represent the eight footprints (FP).

cell aggregation.

To summarize, the first six months of OCO-3 SIF were analyzed and compared to SIF retrieved from OCO-2 for the same time period. There is good overall agreement for relative SIF, especially when full spatial overlaps of scenes are considered. These early results indicate that the SIF scientific community will find the OCO-3 vEarly SIF dataset to be of comparable quality as OCO-2 SIF.

6. OCO-3 vEarly XCO$_2$

In this section the first set of OCO-3 XCO$_2$ estimates from the Atmospheric Carbon Observations from Space (ACOS) retrieval algorithm are presented. The methods used to derive quality filters/flags
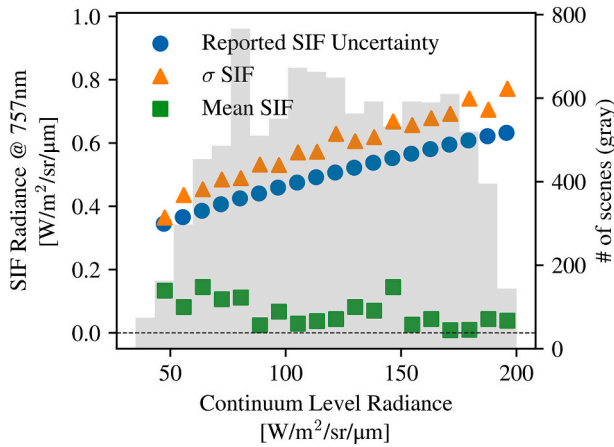
Fig. 16. Theoretical uncertainty of the retrieved SIF (blue circles) and true scatter of SIF (orange triangles) as a function of the continuum level radiance, using scenes measured over the Sahara desert (September 2019). Green squares represent the mean SIF of each bin, showing that the bias-corrected SIF is, on average, close to zero (< 0.15 W/m^2/sr/um) after the bias correction procedure. Only footprint 5 is shown here. (For interpretation of the references to colour in this figure legend, the reader is referred to the web version of this article.)
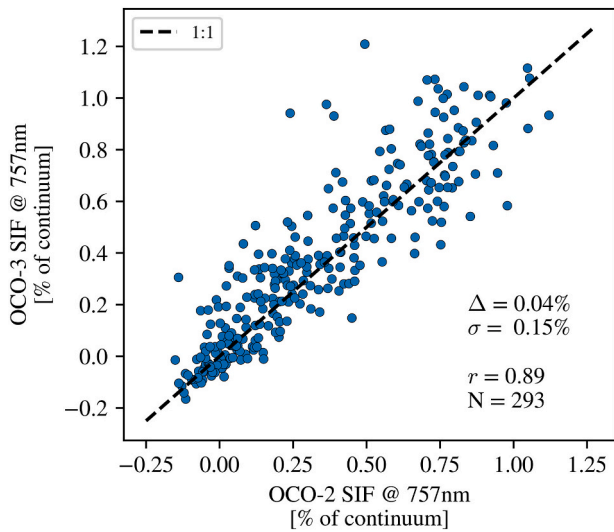

Fig. 17. Comparison between OCO-2 (nadir only) and OCO-3 SIF, aggregated on a grid cell level, taking into account only those cells which exhibit a similar average scene brightness.

(QFs) and bias correction (BC) for the vEarly XCO$_2$ are discussed here and in Appendix B. The initial performance of the XCO$_2$ is evaluated for all four observation modes (ND, GL, TG and SAM) for the time period August through mid-October 2019, and recommendations are provided as to use of the data for scientific analysis. The OCO-3 vEarly products are publicly available through the NASA Goddard Earth Science Data and Information Services Center (GES DISC) for distribution and archiving (http://disc.sci.gsfc.nasa.gov/). Due to residual pointing errors and radiometric calibration inaccuracies in the vEarly product, as well as a limited sample size, a rigorous comparison against OCO-2 XCO$_2$ and time-of-day sampling is deferred to a forthcoming manuscript once the v10 product is available.

6.1. L2FP XCO$_2$ retrieval algorithm

Build 8 (b8) of the ACOS L2FP algorithm was described in (O'Dell et al., 2018), including detailed methodology of the QF and BC
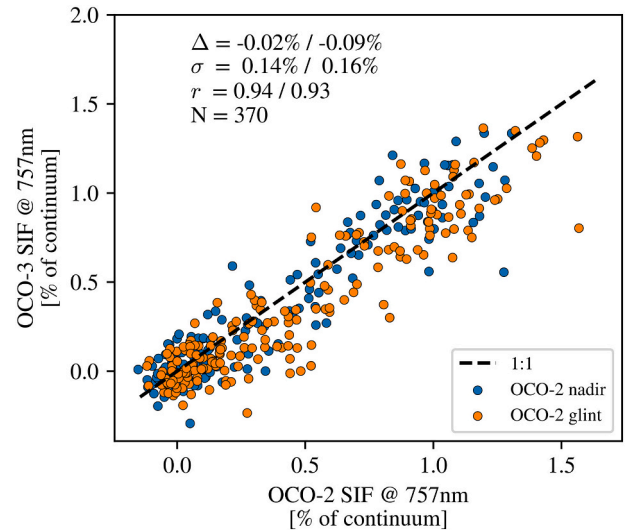
Fig. 18. Similar to Fig. 17, however each point represents a cluster of scenes which have spatial overlap between OCO-2 and OCO-3. SIF retrievals from both nadir and glint observation modes for OCO-2 were utilized. The mean (Δ), standard deviation (σ) and Pearson correlation coefficient (r) are shown for nadir/glint respectively. All OCO-3 scenes are in nadir viewing mode.

techniques. A number of minor adjustments were made to the Build 9 (b9) software, as discussed in (Kiel et al., 2019). Specifically, no changes were made to the L2FP algorithm, but rather a pointing error was corrected via updates to the geolocation, which affected the meteorological resampling. L2Lite files, containing bias corrected and quality flagged XCO$_2$ were generated post-facto. The generation of the OCO-2 v9 data products terminated at the end of January 2020, at which time the b10 build of the L2 software replaced b9 in the production pipeline.

The first version of the OCO-3 data product used the more recent ACOS b10 software, which includes (i) use of the ABSCO v5.1 trace gas spectroscopic parameters, (ii) an improved solar continuum model, (iii) improved aerosol priors from GEOS5-FP-IT with tighter constraints (Nelson and O'Dell, 2019), (iv) an updated CO$_2$ prior in agreement with the forthcoming TCCON GGG2020 software, (v) a quadratic fit for the land surface albedo, and (vi) a loosened SIF prior constraint (Osterman et al., 2020). The resultant OCO-3 data product, vEarly, used instrument calibration refined during IOC (see Section 2.1.4) with initial tuning of the L2FP specifically for OCO-3, e.g., Empirical Orthogonal Functions, as described in Section 3.3 of (O'Dell et al., 2018).

6.2. Quality filtering and bias correction

Similar to XCO$_2$ derived from OCO-2 measurements, a quality filtering procedure is applied to the OCO-3 standard L2FP product to flag soundings that show larger-than-expected scatter or differences in XCO$_2$ relative to truth metrics (O'Dell et al., 2018). Further, a correction of the XCO$_2$ for individual soundings is calculated, aka, a bias correction, since a large fraction of the error in XCO$_2$ correlates with retrieved components of the L2FP state vector. It has been shown that a linear correction demonstrably reduces such errors in XCO$_2$ estimates from space-based measurements (Wunch et al., 2011; O'Dell et al., 2018; Kiel et al., 2019). The L2FP standard product is repackaged into a lightweight set of daily summary files, the so called L2Lite files, containing a greatly reduced set of variables, and including the QFs and BC XCO$_2$ values. Details of the the QF/BC procedures as applied to OCO-3 vEarly are provided in Appendix B.

In short, the vEarly quality filters pass $\simeq 55\%$ of land soundings and $\simeq 65\%$ of water soundings, compared to pass rates of 31% for land and 55% for water on the OCO-2 v8 product as reported in (O'Dell et al.,
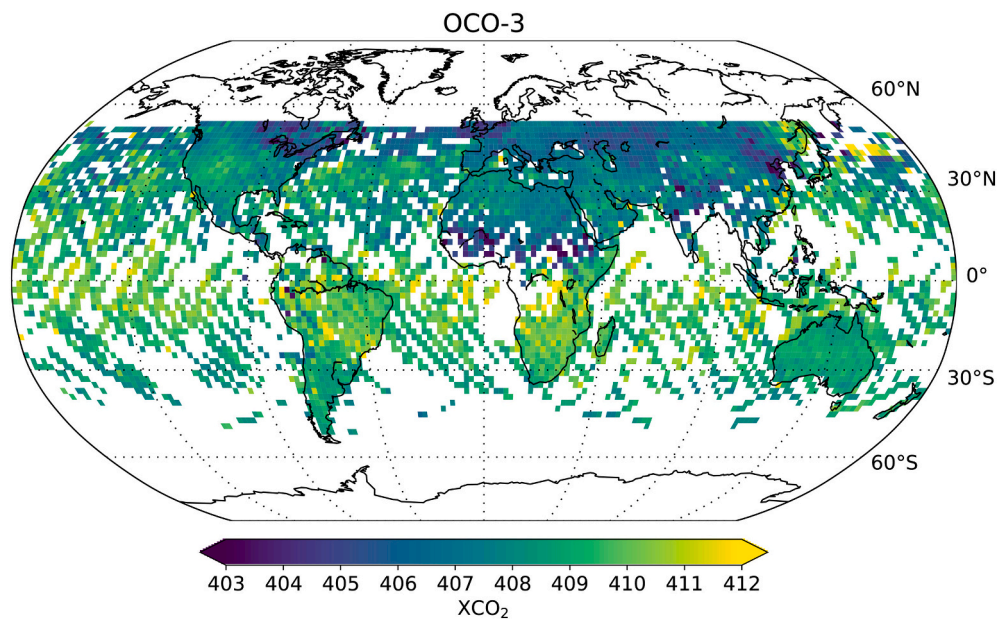
Fig. 19. The good quality OCO-3 vEarly XCO_2 between August and October 2019 aggregated into $2° \times 2°$ latitude/longitude bins.

2018). The QF pass rates were slightly higher for v9 (OCO-2 Science Team et al., 2018) as reported in (Kiel et al., 2019). After QF and BC, the vEarly NL XCO_2 are biased by 0.18 ppm relative to the TCCON truth proxy, with a RMSE of $\simeq 1.1$ ppm, on par with OCO-2 v9. The SAM/TG data also have a RMSE of $\simeq 1$ ppm versus the small area approximation (SAA) truth proxy, similar to OCO-2 v9. After QF and BC, the GW observations have a rather large RMSE of 2.0 ppm versus their SAA truth proxy. This is out-of-family with the OCO-2 v9 results, which had a RMSE of < 1 ppm versus the truth proxy.

6.3. Evaluation of vEarly XCO_2 and recommended usage

Overall, the OCO-3 vEarly good quality and bias corrected XCO_2 data shows broad spatial coverage over much of the land areas between $55°$ N and $55°$ S as seen in Fig. 19. Exceptions are seen over the tropical regions, e.g., central Africa, the northern Amazon, and coastal India and southeast Asia, which are likely impacted by cloud and aerosol contamination, i.e., the quality filtering may not be aggressive enough in these regions. The expected latitudinal gradient in XCO_2 is observed, with lower concentrations in the northern hemisphere due to CO_2 uptake by the biosphere during the late summer and early autumn. Overall, the NL data exhibits characteristics on par with OCO-2 v9, although it is recommended to avoid using measurements over regions of variable topography, i.e., mountainous regions, due to the known pointing errors in vEarly.

The good quality vEarly coverage over water is more sparse than over land between August and October 2019, as seen in Fig. 19. This is mainly due to the early mission glint off-pointing restrictions to avoid over-saturation of the detectors, which lead to much of the data volume being collected in nadir viewing mode. In addition, the often unfavorable polarization alignment yielded a considerable number of soundings with lower than expected SNR, especially in the SCO2 band. These two issues were discussed in Section 4.3. The density of good quality soundings is higher over the northern extra-tropics compared to the tropics and the southern ocean. However, the RMSE is $\simeq 2$ ppm versus the SAA truth proxy, as described in 6.2. This is much higher than the $\simeq 1$ ppm RMSE for OCO-2 v9 versus truth. In addition, an XCO_2 bias is seen between ascending and descending orbits (not shown), which requires further investigation. For all of these reasons, the use of the vEarly GW data is not recommended for scientific analysis.

The bias correction process attempts to account for spurious

differences between land and ocean XCO_2 values by use of separate land and ocean scaling factors, as discussed in Appendix B.5. For OCO-3 vEarly, the scaling factors were set to 1 due to the relative paucity of data available during early analysis. The remaining land-ocean bias in vEarly is $\simeq 0.25$ ppm between $15°$ N and $55°$ S and $\simeq 1.5$ ppm north of $15°$ N. This contrast is currently under investigation, but might be driven by the time of year and strong biospheric CO_2 uptake in the northern hemisphere. The forthcoming v10 product will allow for full characterization of the global scaling parameters, which are anticipated to mitigate the land-ocean contrast, believed to be a spurious feature of the retrieval algorithm.

Linking XCO_2 enhancements identified by satellites with fossil fuel emission estimates from emission inventories and high resolution model simulations is an area of active research, e.g., (Janardanan et al., 2016; Nassar et al., 2017; Zheng et al., 2019; Reuter et al., 2019; Wu et al., 2020; Ye et al., 2020), to which the new OCO-3 SAMs will contribute. Many SAMs are taken coincident with ECOSTRESS measurements (Fisher et al., 2020), over SIF study regions (Yang et al., 2018), and TCCON and COCCON validation sites (Wunch et al., 2011; Frey et al., 2019). However, the majority of SAMs were taken over fossil fuel targets, including mega-cities and power plants, several of which indicate a local enhancement in XCO_2.

Nitrogen dioxide (NO_2) is released into the atmosphere as a by-product of fossil fuel combustion and can help to identify CO_2 emission hot spots (Reuter et al., 2019). To illustrate this, the left panel of Fig. 20 shows QF and BC XCO_2 for a SAM over Esfahan Iran taken on 24 December 2019. An enhancement in the XCO_2 of $\simeq 1-2$ ppm is observed directly over the city. This is in good spatial agreement with TROPOMI's NO_2 measurements that were taken $\simeq 90$ s after the OCO-3 overpass, as seen in the right panel of Fig. 20.

A spurious feature seen in some vEarly SAMs (not shown) are swath-to-swath bias that are not corrected by the BC procedure. These biases may be driven by the viewing geometries coupled with the polarization angle dependencies in the PMA. Further investigation is on-going. The RMSE between the vEarly SAM/TG data and the truth proxy ($\simeq 1$ ppm) is comparable to the RMSE between OCO-2 v9 TG mode observations and its truth proxy. This data set is likely useful for early studies of spatial patterns and urban gradients. However, caution should be used in interpreting the vEarly SAM and TG data for emissions estimates.

Overall, OCO-3 vEarly XCO_2 shows reasonable performance for all viewing modes at the early stage of the mission. The NL dataset is the
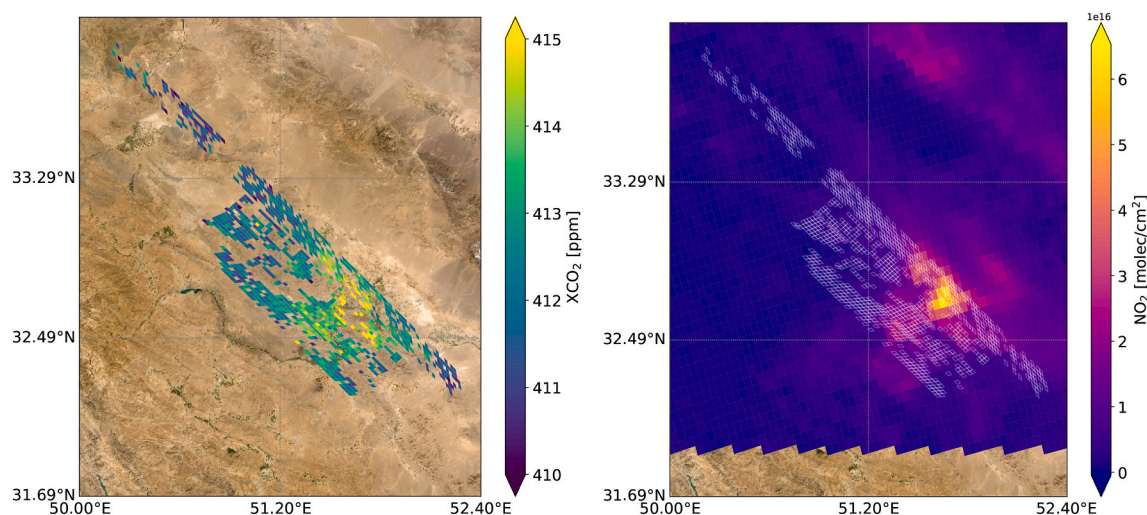
Fig. 20. An OCO-3 vEarly XCO$_2$ SAM observation taken over Esfahan (Iran) on 24 December 2019 (left panel). TROPOMI NO$_2$ over the same region measured $\simeq$ 90 s after the OCO-3 overpass (right panel). White rectangles indicate the position of the OCO-3 footprints.

most robust and well characterized, containing the smallest errors relative to its truth proxy. The vEarly SAM and TG datasets will allow for some earlier investigations into city-scale XCO$_2$ gradients, but should be interpreted with some caution until the remaining pointing errors can be corrected. The vEarly GW dataset does not compare well to its truth proxy, but this is likely due in significant part to PMA control issues early in the mission precluding many high quality glint observations. A more comprehensive OCO-3 data release, anticipated by early in 2021, version 10 (v10), will contain updated L1b calibration, refinement of the geolocation, softening of the early mission glint off-pointing restrictions, tuning of the ACOS b10 L2 algorithms (preprocessors, SIF, L2FP XCO$_2$), and updated quality filtering and bias correction. In addition, a more detailed validation and evaluation of OCO-3 v10 XCO$_2$ will be conducted against TCCON, COCCON, and model data, as well as cross comparisons against OCO-2, and analysis of the varied time of day sampling (Kiel, in prep.).

7. Summary

The OCO-3 SIF and XCO$_2$ data products are rapidly maturing. The heritage of the OCO-2 mission allowed the team to apply code and analysis that had been developed for OCO-2, resulting in rapid progress early in the mission. This paper reports on the early mission activities of OCO-3 during the first 8 months on-orbit, including calibration, the actual experience of operations on the ISS, and the key features in the vEarly data release. Early instrument calibration activities provided an update to the spectrometer bad pixel map, while characterization of the radiometric degradation is currently based on in-flight lamp measurements. This will be updated in a future release when additional measurements are available such as vicarious calibration and lunar observations. On-orbit pointing calibration of the pointing mirror assembly and flight software updates removed large pointing errors. Residual pointing errors in the vEarly data are typically less than 1 footprint (order 2 km) for nadir viewing. For larger off-nadir angles, residual pointing errors are between 1 km and 4 km. The mission operations and planning for calibration and science measurements were updated during the first 8 months to more effectively manage scheduling around arriving and departing vehicles and other ISS interruptions. A number of instrument faults were experienced early in the mission, especially in the first three months, but they have been investigated and are now avoided with updated observation planning strategies. The ABP cloud prescreener performance for OCO-3 was evaluated against GOES-ABI and showed results that are similar to the OCO-2 cloud screening compared to MODIS.

The vantage point of the ISS creates unique patterns of sampling, with data density varying with latitude and time. OCO-3 samples between 6 h before local noon to 6 h after local noon, covering latitudes of 52° N to 52° S. The OCO-3 sampling is across a wide range of polarization angles, and the pattern is related to the ISS beta angle, the angle between the ISS orbital plane and the Earth-Sun vector. This results in a wide dynamic range of signal, and therefore signal to noise, for the glint measurements. In addition, a large glint offset was used in the early mission data collection before pointing errors were determined. Comparison of the SNR across all three bands and glint and nadir measurements show that generally the OCO-3 ABO2 spectral band has comparable SNR to OCO-2, while the WCO2 and SCO2 spectral bands have somewhat lower SNR compared to OCO-2.

SIF retrievals from OCO-3 show somewhat higher correction factors compared to OCO-2. This is likely related to instrument calibration errors. Direct comparisons of OCO-2 and OCO-3 SIF show comparable performance – the true scatter in the retrieved SIF is 10–20% higher than the reported uncertainty, as was seen in OCO-2. Direct OCO-2 to OCO-3 SIF comparisons with gridded data show a small bias and a correlation coefficient of 0.89. In a comparison of OCO-2 and OCO-3 data with close spatial coincidence, the correlation is 0.94 and 0.93 for OCO-2 nadir-land and OCO-2 glint-water, respectively.

Quality filtering and bias correction have been developed for the vEarly L2FP XCO$_2$ data following the methodology developed for OCO-2. The filters use parameters that are similar to those used for OCO-2 v9 and remove $\simeq$ 45% (35%) of land (water) soundings. The bias correction also relies on L2FP variables similar to those used in the OCO-2 v9 bias correction. A number of truth proxies are used in this analysis, including the TCCON validation data, small areas, and SAMs that are free from significant emission sources. After filtering and bias correction, the NL data has a bias of 0.18 ppm and an RMSE of 1.1 ppm relative to TCCON, which is comparable to the OCO-2 v9 values. The glint-water data was difficult to characterize due to early mission performance issues. An RMSE of $\simeq$ 2 ppm versus a small area truth approximation was determined, compared to < 1 ppm for OCO-2 v9, making the vEarly GW data unfit for scientific analysis.

A new data collection mode, Snapshot Area Mapping (SAM), has been demonstrated by OCO-3. These data collections cover $\simeq$ 80 km $\times$ 80 km in 2 min. An RMSE of $\simeq$ 1 ppm versus a small area truth approximation was determined, in-line with OCO-2 v9 target mode observations. Measurements over fossil fuel emission regions show plume-like features of enhanced XCO$_2$ that often correspond to NO$_2$ enhancements measured by TROPOMI. Further development and analysis of SAMs will be an important and unique contribution of the OCO-3

mission to the carbon cycle science community.

A future release of OCO-3 data (v10) is anticipated by early in 2021. This version will also use the ACOS b10 software build, but will include improvements in instrument calibration, additional pointing corrections, and L2FP algorithm tuning, as well as updated quality filtering and bias correction. A more rigorous validation against TCCON and other truth metrics will be provided at that time.

Declaration of competing interest

We declare no conflicts of interest with this research.

Appendix A. Mission operations

A.1. Routine operations aboard the International Space Station (ISS)

Routine OCO-3 operations are handled by the Mission System Team (MST), which is comprised of three sub-systems: Mission Operations System (MOS), Ground Data System (GDS), and Science Data Operations System (SDOS). Operations are performed in collaboration with the NASA groups that lead the International Space Station activities.

The key tasks for the MST are; (i) instrument commanding, including developing sequences for routine operations, (ii) monitoring the payload health and status, (iii) processing the raw data to usable data products, (iv) and providing the publicly distributed data products. A flow diagram of the various interfaces of the MST is shown in Fig. A1.
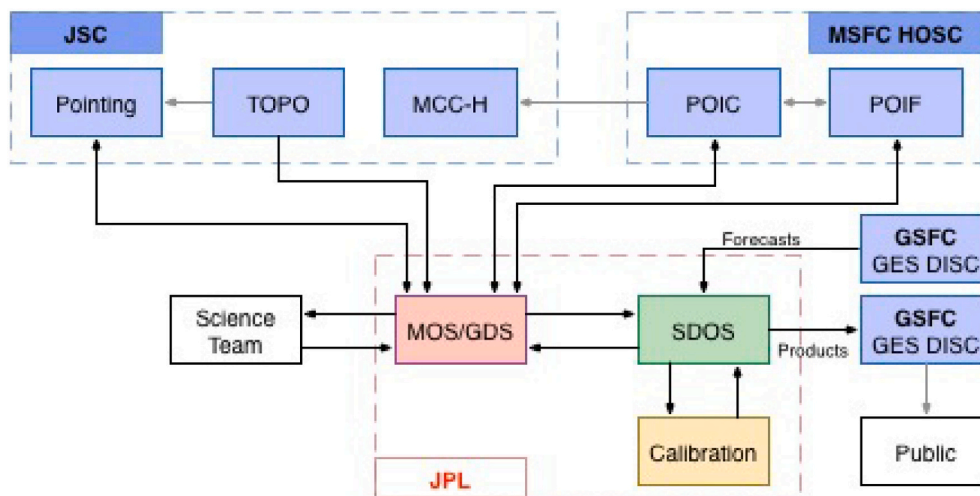

Fig. A1. Flow diagram depicting the major pieces of the OCO-3 Mission System.

MOS is responsible for monitoring and operating the OCO-3 instrument during nominal operations, as well as making and uploading weekly sequences. A library of routinely used sequences and scripts is maintained, e.g. a calibration sequence that collects dark and lamp science data. For sequence planning, OCO-3 needs the ISS ephemeris files (a standardized file that provides the station navigation data) and the lighting files (used to define the orbit boundaries, where each orbit spans midnight-to-midnight) from the Pointing Office at the Johnson Space Center.

Raw data is downlinked from OCO-3 by the GDS. The GDS software is an adaptation of the Advanced Multi-mission Operations System (AMMOS) (Ko et al., 2010) Instrument Toolkit (AIT) (Joyce et al., 2018), which is also used to support other ISS payloads managed by JPL. Health and Status (H &S) telemetry is transmitted from the ISS over 1553, a commonly used standard for spacecraft on-board data handling.

The OCO-3 SDOS system is adapted from the OCO-2 project. It processes the raw telemetry and generates Level 0, Level 1 and Level 2 products. SDOS obtains the Goddard Earth Observing System, Version 5 (GEOS-5) Forward Processing for Instrument Teams (FP-IT) data used to generate the Level 2 meteorology files, which are used to provide apriori information to L2 algorithms. OCO-3 data products are delivered to the Goddard Earth Sciences Data and Information Services Center (GES DISC) for distribution and archive.

A.2. Commanding and sequence planning

MOS conducts uplink activities in the Earth Observing Mission Operations Center (EOMOC) at the Jet Propulsion Laboratory. Commands are generated, verified at JPL, and validated against a command dictionary before being sent to the Payload Operations Integration Center (POIC) at the Marshall Space Flight Center (MSFC). The interface with the Huntsville Operations Support Center (HOSC) at MSFC include both uplink for commanding and downlink for real-time monitoring and to receive science data, discussed in the next section.

The majority of commanding is done with weekly sequences that are generated by CLASP, a JPL scheduling tool for non-agile sensors (Moy et al., 2019). This software utilizes the ephemeris predictions, knowledge of keep-out zones (regions that are unsafe to view when the instrument is operational), and solar zenith angle restrictions. It prioritizes science observing modes according to predefined rules, and develops the timeline of events and the list of commands. Science sequences are then validated by checking time offsets, verifying commands and values against the command dictionary, and then run through the Pointing Control System Simulator (PCSSim). Plots and other checks are reviewed by the team, and any observations that are at risk of violating the glint or keep out zone constraints are then deleted from the weekly sequence.

A.3. Payload health and telemetry

A key task for the MST is to monitor the payload health. The HOSC pushes real-time 1 Hz 1553 payload health and status telemetry to the OCO-3 GDS servers. The data is checked against pre-defined limits, and warnings via emails and text messages are sent to operators if limits are exceeded. The 1553 telemetry data is also queried from the Near Real Time Server (NRT server) every hour to make daily, 2-day and bi-weekly trending reports and plots. These reports and the monitoring limits alleviate the need for operators to remain physically on-console to monitor the instrument.

A.4. Data processing flow

The first step of the data processing stream is to receive the science data and camera imagery from the on-orbit payload. The data flows from the ISS to the HOSC, and is then downloaded to JPL. A dedicated system is used to process the camera data, while another system processes both the ancillary and the raw telemetry data to produce Level 1a products. Then geolocated and calibrated Level 1b products are generated, and finally, the preprocessor and L2 Full Physics (L2FP) algorithms are launched. This pipeline produces what is known as the forward stream, in which current instrument calibration values are used. The resultant products are delivered to the Goddard Earth Sciences Data and Information Services Center (GES DISC).

The lag time on the forward stream is approximately 24 h from the time of measurement to production of the L2FP results. Although these data are of science quality, it has been demonstrated with OCO-2 that both calibration issues in the L1b radiances and biases in the L2FP XCO$_2$ values limit the utility of the forward steam products. Therefore, a retrospective stream has been initiated which uses improved instrument calibration parameters to rederive the L1b radiances prior to running the L2FP retrieval. Then a bias correction and quality filtering are applied (see Section 6) and data are aggregated into the daily L2Lite files which have proven to be the most useful for science applications.

For the vEarly collection, soundings were processed through the L2 software (meteorology resampling, preprocessors, SIF, L2FP XCO$_2$) in the Science Computing Facility (SCF) using the relatively new b10 build. These early data allowed for rapid evaluation of the early mission OCO-3 performance while refinements continued on the geolocation, instrument calibration, and the filtering and bias correction for the more comprehensive v10 data release expected by early in 2021. The vEarly L1b were made available to the public on 30 January 2020 and the L2 products were made available to the public beginning on 4 May 2020. As of August 2020, the vEarly L2Lite file record is also available in daily netCDF format.

A.5. Data collection interruptions

A.5.1. Interruptions due to HOSC activities or anomalies

On numerous occasions, science data collection for OCO-3 has been interrupted by ISS events and operational issues, faulty MOS instructions or payload errors, as listed in Table A1. Some ISS activities present a risk to the OCO-3 instrument, during which the PMA is commanded to point at the calibrator and the instrument in put into standby mode. This is referred to as a no-operation (no-op) period. For example, during ISS purging activities, when there is concern about gas contamination of the OCO-3 instrument. In addition, vehicles visiting the ISS can pass through the OCO-3 FOV and produce extremely bright sun-glint signals that might damage the instrument FPAs.

No-op periods are inserted into the weekly sequences to accommodate these scheduled activities. However, the ISS schedule can be volatile, with activities often being rescheduled on short notice. Frequently the MOS team is required to quickly update the sequences to protect the instrument. Reboots, arrival and departure of vehicles, and astronaut extravehicular activity have resulted in 14 no-op periods between August 2019 and mid-February 2020. These outages range from 27% to 100% of possible orbits, with somewhat lower losses later in the mission, as the team has become more efficient at scheduling no-op periods.

A.5.2. Interruptions due to OCO-3 anomalies

During early operations, there were interruptions to data collection due to tripping faults in the pointing control software, and issues with GPS and SRU validity checks. Science data collection was impacted by these faults in early August 2019 (25 orbits), September 2019 (1–3 orbit), early November 2019 (73 orbits) and late January 2020 (15 orbits). As noted in Section 2.1.2, in October and November of 2019, science data collection was interrupted during PMACal activities and decontamination cycles, which resulted in a few weeks of downtime.

There are also periods when all data was collected in nadir mode. This mode yields useful science data over land, but has insufficient SNR for XCO$_2$ retrievals over water surfaces. Nadir-only mode has been used during investigations of trips or faults in the PCS (October 2019 and January 2020) and when the sun in almost directly overhead, such that the sun glint spot moves rapidly and cannot be tracked for glint observations. All time periods of nadir-only operations are noted in Table A2 in Appendix A.

Table A1
Interruptions to OCO-3 during early operations aboard the ISS.

Index	Start date	End date	Cause of outage	# Orbits Lost	# Orbits Possible	% Orbits Lost	Responsible Party (MOS/ISS)
1.	12-Aug-2019	16-Aug-2019	ISS reboost	28	78	35.9	ISS
2.	23-Aug-2019	27-Aug-2019	Docking 60S	66	66	100.0	ISS
3.	27-Aug-2019	28-Aug-2019	Sequence planning; PMA flip-line issue	25	27	92.6	MOS
4.	25-Sep-2019	28-Sep-2019	Docking 61S & HTV capture	27	62	43.6	ISS
5.	29-Sep-2019	05-Oct-2019	GPS outage; sequence abort	103	103	100.0	MOS
6.	09-Oct-2019	14-Oct-2019	EVA & robotic arm & purge	23	93	24.73	ISS
7.	19-Oct-2019	27-Oct-2019	Packet loss	139	140	99.3	ISS
8.	28-Oct-2019	31-Oct-2019	FSW update (54 orbits) & HTV pre-grapple (8 orbits)	62	62	100.0	MOS ISS
9.	01-Nov-2019	06-Nov-2019	PMA overshoot (73 orbits) & Launch/release (21 orbits)	94	94	100.0	MOS ISS

Table A1 (*continued*)

Index	Start date	End date	Cause of outage	# Orbits Lost	# Orbits Possible	% Orbits Lost	Responsible Party (MOS/ISS)
10.	07-Nov-2019	27-Nov-2019	PMACal and decon	325	325	100.0	MOS
11.	29-Nov-2019	29-Nov-2019	Undocking 73P	5	16	31.3	ISS
12.	02-Dec-2019	05-Dec-2019	Cargo extraction	39	62	62.9	ISS
13.	08-Dec-2019	09-Dec-2019	Capture SpX 19, Docking 74P	9	31	29.0	ISS
14.	21-Dec-2019	31-Dec-2019	Dockings and ISS reboost	46	172	26.7	ISS
15.	05-Jan-2020	07-Jan-2020	Unberth SpX 19	18	46	39.1	ISS
16.	15-Jan-2020	15-Jan-2020	Battery EVA	8	15	53.3	ISS
17.	18-Jan-2020	21-Jan-2020	Instrument safe OCO-3	15	62	24.2	MOS
18.	23-Jan-2020	27-Jan-2020	ISS Russian BAD data stream	54	62	87.1	ISS
19.	31-Jan-2020	01-Feb-2020	Survey Setup IDA3 & Release NG12	15	31	48.4	ISS
20.	03-Feb-2020	06-Feb-2020	Packet loss	58	62	93.6	ISS
21.	16-Feb-2020	18-Feb-2020	Capture and install NG-13	15	47	31.91	ISS

Table A2

OCO-3 glint viewing mode interruptions during early operations. The two right-most columns give the number of orbits collected in ND-only viewing mode and those in combined ND + SAM + TG viewing modes, respectively.

Index	Start date	End date	Reason for no glint	# Orbits (ND only)	# Orbits (ND + SAM + TG)
1.	04-Sep-2019	22-Sep-2019	Viewing constraints	209	99
2.	05-Oct-2019	09-Oct-2019	GPS outage and obs near PMA flip-line	20	49
3.	07-Dec-2019	20-Dec-2019	ISS activities and high solar beta angle	207	0
4.	27-Dec-2019	31-Dec-2019	MOS validation failure during no-ops period	71	0
5.	01-Jan-2020	06-Jan-2020	MOS validation failure during no-ops period	90	0
6.	18-Jan-2020	29-Jan-2020	OCO-3 instrument safe & C1 constraint violations	115	0
7.	07-Mar-2020	16-Mar-2020	viewing constraints at high solar beta angle	52	23

Appendix B. Quality filtering and bias correction of OCO-3 vEarly

B.1. Truth proxy training data sets

To derive QF and BC, the methods described in Section 4 of (O'Dell et al., 2018) were followed. The retrieved XCO_2 was compared to an independent estimate of XCO_2, a so-called truth proxy. For OCO-3 vEarly, three truth proxy data sets were used; TCCON for NL, a small area approximations (SAAs) for GW, and a SAA for TG and SAM mode observations. Additional details on the SAA methodology are documented in Section 4.1.2 of (O'Dell et al., 2018).

For NL observations, the truth proxy consisted of TCCON data from 16 stations using the GGG2014 data set (Wunch et al., 2015) spanning August to October 2019 and ∼ 55° N to ∼ 45° S in latitude. A listing of the TCCON stations with the relevant citations is given in Table B1. A similar coincidence criteria as that used by (O'Dell et al., 2018) was implemented to match air masses observed by TCCON and OCO-3. In total ≃ 80 k coincident soundings between OCO-3 and TCCON were used in the training data set.

Table B1

Stations used in the TCCON truth proxy data set for the validation of OCO-3 vEarly.

TCCON station	Reference
Bremen, Germany	Notholt et al. (2014)
Caltech, Pasadena, CA, USA	Wennberg et al. (2014a)
Darwin, Australia	Griffith et al. (2014a)
Edwards (Armstrong), CA, USA	Iraci et al. (2016)
Garmisch, Germany	Sussmann and Rettinger (2014)
Izaña, Tenerife, Spain	Blumenstock et al. (2014)
Karlsruhe, Germany	Hase et al. (2014)
Lamont, OK, USA	Wennberg et al. (2016)
Lauder, New Zealand	Pollard et al. (2019)
Orléans, France	Warneke et al. (2014)
Paris, France	Te et al. (2014)
Park Falls, WI, USA	Wennberg et al. (2014b)
Rikubetsu, Japan	Morino et al. (2014a)
Saga, Japan	Kawakami et al. (2014)
Tsukuba, Japan	Morino et al. (2014b)
Wollongong, Australia	Griffith et al. (2014b)

The SAA for GW observations makes use of the low spatial variability of XCO_2 over small regions (up to 100 km) and short time spans (≃ 10 s). Here, we define continuous glint segments of up to 70 km length along-track as small areas. Between August and October 2019, approximately 3000

small areas over water were used as a truth proxy for GW observations.

For TG and SAM mode observations, a set of SAMs over SIF and deserts were selected for the truth proxy. In contrast to observations over fossil fuel targets, XCO_2 concentrations over ecological and desert scenes of the size of 80 km × 80 km and collected over a ≃ 2 min time interval, can be assumed as nearly constant, providing a *true* XCO_2. Variations of single soundings from this truth are used to identify spurious and systematic biases in the L2FP estimates of XCO_2. Currently, remaining uncertainties in the knowledge of the pointing of OCO-3 (see discussion in Section 2.1.3) may introduce biases in the XCO_2 retrievals, especially in regions with large topographic variations (Kiel et al., 2019). These biases are more prominent in the data measured at large PMA elevation angles typical during TG and SAM mode observations. Therefore, we only include SAMs in the truth proxy with low topographic variations (less than 200 m over the entire scene). In total, 47 SAMs contribute to the SAA truth proxy for SAM and TG mode observations. An overview of the truth proxies is given in Table B2.

Table B2
Overview of the truth proxy training datasets for OCO-3 vEarly.

Name	Mode	N ($\times 10^3$)	Details
TCCON	NL	~ 80	GGG2014 (Wunch et al., 2015)
SAA	GW	~ 400	areas < 100 km along-track
SAA	TG/SAM (land)	~ 66	SIF & desert

B.2. Quality filters

Using the truth proxies defined in Section Appendix B.1, soundings with XCO_2 error that are deemed too large relative to truth are flagged by threshold-based filters according to the methodologies developed in (Mandrake et al., 2013; Eldering et al., 2017; O'Dell et al., 2018). Note that all soundings are retained in the Lite file product; each is assigned either a good (QF = 0) or bad (QF = 1) value. It is incumbent upon individual researchers to choose which soundings to retain for analysis, but those with QF = 1 should be interpreted with caution.

Table B3 summarizes the viewing-mode dependent variables and limits that are used to define the OCO-3 vEarly QFs. A total of twenty four (24) variables were used, with seven (7) common to all three viewing modes. For each variable, the threshold limits differ by observation mode. For example, the upper limit of the surface roughness (ρ) has a lower value for SAMs than for ND observations, removing soundings that are affected by topography related biases. The variables and values in this table can be compared to those for OCO-2 v8 reported in table A1 of (O'Dell et al., 2018) and those for OCO-2 v9 reported in table 5 of (Kiel et al., 2019). Although a number of the variables are common to all, e.g., IDP CO_2 and H_2O ratios, L2FP dp, ABP dp, there are substantial differences in the OCO-3 vEarly, one of which is less reliance on aerosol related variables compared to OCO-2 v8/v9.

For SAM observations, which are always over land, the NL variables plus an additional 5 variables, for a total of 18, were selected. The variables selected to filter the GW observations have some commonality with the land filters (7 are the same), but includes a few new ones, for a total of 15 variables. The quality filters pass ≃ 55% of the soundings over land and ≃ 65% over water. This compares to pass rates of 31% for land and 55% for water on the OCO-2 v8 product, as reported in section 4.2 of (O'Dell et al., 2018). An additional 10–15% pass rate was reported in (Kiel et al., 2019) for OCO-2 v9, bringing the numbers slightly more in alignment with the OCO-3 vEarly results.

Table B3
Quality filter variables and limits for the OCO-3 vEarly XCO_2 quality flag. Most variables are from the L2FP algorithm, except where noted.

Variable	Description	Unit	NL	SAM (land)	GW
IDP CO_2 ratio	Definition given in Section 3.2		[1.00, 1.05]	[1.00, 1.04]	[1.00, 1.03]
IDP H_2O ratio	Definition given in Section 3.2		[0.875, 1.050]	[0.80, 1.05]	[0.90, 1.05]
$\mathscr{R}_{ABO2}^{RMS}$	The relative RMS error of the spectral fit residuals in the ABO2 spectral band	[%]	[0, 0.0035]	[0, 0.0025]	[0, 0.004]
$\mathscr{R}_{WCO2}^{RMS}$	Same as above for the WCO2 spectral band	[%]		[0, 0.0025]	
$\mathscr{R}_{SCO2}^{RMS}$	Same as above for the SCO2 spectral band	[%]	[0, 0.0075]	[0, 0.005]	[0, 0.006]
χ_{O2}^2	The reduced chi-squared fit statistic in the ABO2 spectral band				[0, 1.5]
χ_{SCO2}^2	Same as above for the SCO2 spectral band				[0, 1.5]
α_{ABO2}	Retrieved albedo in the ABO2 spectral band				[0.005, 0.040]
α_{WCO2}	Same as above for WCO2 spectral band				[0, 0.025]
α_{SCO2}	Same as above for SCO2 spectral band				[0.0196, 0.0200]
Λ_{ABO2}^2	BRDF reflectance quadratic coefficient in the ABO2 spectral band	[cm^{-2}]		$[-1.2, 1.0] \times 10^{-7}$	
Λ_{WCO2}^2	Same as above for the WCO2 spectral band	[cm^{-2}]	$[-2.0, 2.1] \times 10^{-6}$	$[-1.0, 1.8] \times 10^{-6}$	
Λ_{ABO2}	BRDF reflectance slope coefficient in the ABO2 spectral band	[cm^{-1}]		$[-8, 1] \times 10^{-5}$	$[-2.0, 0.2] \times 10^{-5}$
Λ_{WCO2}	Same as above for the WCO2 spectral band	[cm^{-1}]	$[-22.5, 2.5] \times 10^{-5}$	$[-25.0, 2.5] \times 10^{-5}$	
Λ_{SCO2}	Same as above for the SCO2 spectral band	[cm^{-1}]	$[-25, 50] \times 10^{-5}$	$[-20, 40] \times 10^{-5}$	$[-4, 10] \times 10^{-5}$
dp	Retrieved minus prior surface pressure in the L2FP algorithm	[hPa]	[−10,2]	[−15, 3]	[−11, 5]
ABP dpcld	Retrieved minus prior surface pressure in the ABP algorithm	[hPa]		[−20,12]	[−15, 5]
$\delta \nabla_{CO2}$	The tropospheric lapse rate of the retrieved CO_2 profile	[ppm]	[−50, 115]	[−50, 70]	[−30, 35]
$\tilde{T}$	Temperature offset relative to the prior	[K]	[0.0, 1.5]	[−0.3, 1.5]	
$\tilde{w}$	Retrieved wind speed	[ms^{-1}]			[0,20]
ρ	Surface roughness (the standard deviation of the surface elevation in the instrument FOV)	[m]	[0, 150]	[0,50]	
τ_{total}	Total aerosol optical depth retrieved by the L2FP algorithm		[0.0, 0.2]	[0.0, 0.3]	
DWS AOD	Combined optical thickness of the dust, water, and sea salt aerosol retrieved by the L2FP algorithm				[0, 0.15]
Ω_{ABO2}	Maximum declocking factor in the ABO2 spectral band		[0.99, 1.01]	[0.99, 1.01]	

B.3. Footprint bias correction

Due to inadequacies in the instrument calibration, OCO-2 and OCO-3 contain small biases in the retrieved XCO_2 at the individual footprint level. Recall that each measurement frame is comprised of 8 spatial footprints. Footprint biases are evaluated using the SAM truth proxy for land observations and the glint truth proxy for soundings over water. For all frames that contain all eight footprints, the footprint bias is calculated as the difference of each footprint from the median XCO_2 of the frame. OCO-3 footprint biases are similar for land and water soundings and only differ slightly in magnitude but not sign. The largest bias is estimated for footprint seven ($\simeq -0.55$ ppm) which is consistent with pre-flight tests. Overall, the results are of approximately the same magnitude as those reported for OCO-2 v8 in Section 4.3.2 of (O'Dell et al., 2018), which spanned -0.36 to $+0.34$. The correction factors given in Table B4 are applied to OCO-3 vEarly XCO_2, minimizing footprint dependent biases, which is crucial for scientific studies on local scales.

Table B4
Estimates of the eight OCO-3 footprint (FP) biases for land and ocean observations (given in ppm).

Mode	FP1	FP2	FP3	FP4	FP5	FP6	FP7	FP8
Land (all)	-0.30	0.07	0.08	-0.05	0.39	0.28	-0.59	-0.05
GW	-0.54	0.16	0.10	0.00	0.54	0.23	-0.49	-0.30

B.4. Parametric bias correction

The parametric bias correction attempts to correct for biases in XCO_2 that are functionally related to a given parameter in the retrieval state vector (Wunch et al., 2017; O'Dell et al., 2018). Here, the mode-dependent parametric bias ($XCO_{2,\ para}$) has the form of a multivariate regression:

$$XCO_{2,para} = \sum_i c_i (p_i - p_{i,\mathrm{ref}}) \tag{B.1}$$

Regression coefficients are denoted as c_i and represent the dependence of the footprint corrected XCO_2 ($XCO_{2,\ fp}$) to the selected parameter p_i. The corresponding reference values are denoted as $p_{i,\ \mathrm{ref}}$. The bias-corrected ($XCO_{2,\ bc}$) is calculated as:

$$XCO_{2,bc} = XCO_{2,fp} - XCO_{2,para} = XCO_{2,fp} - \sum_i c_i (p_i - p_{i,\mathrm{ref}}), \tag{B.2}$$

with the mode dependent coefficients and reference values summarized in Table B5.

For vEarly NL observations, three different L2FP parameters account for the largest fraction of variability in XCO_2: dp, Λ_{WCO2}, and DWS AOD (see descriptions in Table B3). For SAMs and GW observations, dp and $\delta \nabla_{CO_2}$ contribute to the parametric bias correction. The $\delta \nabla_{CO_2}$, commonly referred to at the "CO_2 grad del", represents the tropospheric lapse rate of the retrieved CO_2 profile and is defined as the difference in the retrieved CO_2 between the surface and the retrieval pressure level at 0.6 times the surface pressure minus the same quantity for the prior profile. See eq. 5 in (O'Dell et al., 2018).

After filtering and bias correction, the root-mean-squared-error (RMSE) between OCO-3 XCO_2 and the truth proxy data set is reduced from 2.94 ppm to 1.51 ppm for NL observations, from 2.60 ppm to 0.98 ppm for SAM observations, and from 2.90 ppm to 2.00 ppm for GW observations.

B.5. Global scaling factor

Global scaling factors for both land and water are used to correct for an overall XCO_2 bias and to tie the XCO_2 to the WMO trace gas standard scale. Typically, the factor is derived for land by comparing TG mode observations over TCCON sites. TCCON serves as a link between the WMO trace gas standard scale and satellite measurements. At this early stage of the mission, there are a very limited number of coincident TCCON and OCO-3 target mode observations available. However, OCO-3 overpasses in ND mode over TCCON sites (which fulfill the coincident criteria described in Section Appendix B.1) indicate a global scaling factor close to unity.

For GW observations, at this early stage, there are too few coincident soundings between TCCON over water and OCO-3 to derive a global scaling factor. We therefore adapt a global scaling factor of one (1) for all observation modes for vEarly and plan to revisit the derivation of a global scaling factor during the development of the OCO-3 v10 product.

Table B5
Parametric bias correction coefficients and reference values for vEarly.

NL	dp	Λ_{WCO2}	DWS AOD
Coefficients	-0.212 ppm hPa^{-1}	-4.931 ppm	-11.689 ppm
Reference values	-4.716 hPa	0.255	0.016
SAM/TG (land)	dp	$\delta \nabla_{CO_2}$	
Coefficients	-0.081 ppm hPa^{-1}	-0.008	
Reference values	-4.766 hPa	29.405 ppm	
GW	dp	MIN($\delta \nabla_{CO_2}$, 2.6)	
Coefficients	-0.208 ppm hPa^{-1}	0.16	
Reference values	-3.36 hPa	2.6 ppm	

References

Aben, I., Hasekamp, O., Hartmann, W., 2007. Uncertainties in the space-based measurements of CO_2 columns due to scattering in the Earth's atmosphere. J. Quant. Spectrosc. Radiat. Transf. 104, 450–459. https://doi.org/10.1016/j.jqsrt.2006.09.013.

Alonso, L., Gomez-Chova, L., Vila-Frances, J., Amoros-Lopez, J., Guanter, L., Calpe, J., Moreno, J., 2008. Improved Fraunhofer line discrimination method for vegetation fluorescence quantification. IEEE Geosci. Remote Sens. Lett. 5 (4), 620–624. https://doi.org/10.1109/LGRS.2008.2001180.

Blumenstock, T., Hase, F., Schneider, M., Garcia, O.E., Sepulveda, E., 2014. TCCON Data from Izana (ES), Release GGG2014R0, TCCON Data Archive, Hosted by CaltechDATA. https://doi.org/10.14291/tccon.ggg2014.izana01.R0/1149295.

Boesch, H., Brown, L., Castano, R., Christi, M., Connor, B., Crisp, D., Eldering, A., Fisher, B., Frankenberg, C., Gunson, M., Granat, R., McDuffie, J., Miller, C., Natraj, V., O'Brien, D., O'Dell, C., Osterman, G., Oyafuso, F., Payne, V., Polonsky, I., Smyth, M., Spurr, R., Thompson, D., Toon, G., January 2019. Orbiting Carbon Observatory-2 & 3 level 2 full physics retrieval algorithm theoretical basis. In: Algorithm Theoretical Basis Document D-55207. Jet Propulsion Laboratory URL. https://disc.gsfc.nasa.gov/datacollection/OCO3_L2_Standard_EarlyR.html.

Bryant, N., Bunch, W., Fretz, R., Kim, P., Logan, T., Smyth, M., Zobrist, A., 2012. Obtaining Accurate Change Detection Results from High-Resolution Satellite Sensors. IEEE Applied Imagery Pattern Recognition Workshop (AIPR), Washington, DC. https://doi.org/10.1109/AIPR.2012.6528199.

Butz, A., Hasekamp, O., Frankenberg, C., Aben, I., 2009. Retrievals of atmospheric CO_2 from simulated space-borne measurements of backscattered near-infrared sunlight: accounting for aerosol effects. Appl. Opt. 48, 3322–3336. https://doi.org/10.1364/AO.48.003322.

Cox, C., Munk, W.H., 1954. The measurement of the roughness of the sea surface from photographs of the sun's glitter. J. Opt. Soc. Am. A 44, 838–850. https://doi.org/10.1364/JOSA.44.000838.

Crisp, D., Pollock, H.R., Rosenberg, R., Chapsky, L., Lee, R.A., Oyafuso, F.A., Frankenberg, C., O'Dell, C.W., Bruegge, C.J., Doran, G.B., Eldering, A., Fisher, B.M., Fu, D., Gunson, M.R., Mandrake, L., Osterman, G.B., Schwandner, F.M., Sun, K., Taylor, T.E., Wennberg, P.O., Wunch, D., 2017. The on-orbit performance of the Orbiting Carbon Observatory-2 (OCO-2) instrument and its radiometrically calibrated products. Atmos. Meas. Tech. 10, 59–81. https://doi.org/10.5194/amt-10-59-2017.

Crowell, S., Baker, D., Schuh, A., Basu, S., Jacobson, A.R., Chevallier, F., Liu, J., Deng, F., Feng, L., McKain, K., Chatterjee, A., Miller, J.B., Stephens, B.B., Eldering, A., Crisp, D., Schimel, D., Nassar, R., O'Dell, C.W., Oda, T., Sweeney, C., Palmer, P.I., Jones, D.B.A., 2019. The 2015–2016 carbon cycle as seen from OCO-2 and the global in situ network. Atmos. Chem. Phys. 19 (15), 9797–9831. https://doi.org/10.5194/acp-19-9797-2019. URL. https://www.atmos-chem-phys.net/19/9797/2019/.

Eldering, A., O'Dell, C.W., Wennberg, P.O., Crisp, D., Gunson, M.R., Viatte, C., Avis, C., Braverman, A., Castano, R., Chang, A., Chapsky, L., Cheng, C., Connor, B., Dang, L., Doran, G., Fisher, B., Frankenberg, C., Fu, D., Granat, R., Hobbs, J., Lee, R.A., Mandrake, L., McDuffie, J., Miller, C.E., Myers, V., Natraj, V., O'Brien, D., Osterman, G.B., Oyafuso, F., Payne, V.H., Pollock, H.R., Polonsky, I., Roehl, C.M., Rosenberg, R., Schwandner, F., Smyth, M., Tang, V., Taylor, T.E., To, C., Wunch, D., Yoshimizu, J., 2017. The Orbiting Carbon Observatory-2: first 18 months of science data products. Atmos. Meas. Tech. 10, 549–563. https://doi.org/10.5194/amt-10-549-2017.

Eldering, A., Taylor, T.E., O'Dell, C.W., Pavlick, R., 2019a. The OCO-3 mission: measurement objectives and expected performance based on 1 year of simulated data. Atmos. Meas. Tech. 12, 2341–2370. https://doi.org/10.5194/amt-12-2341-2019.

Eldering, A., Pollock, R., Lee, R., Rosenberg, R., Oyafuso, F., Crisp, D., Chapsky, L., Granat, R., 2019b. Orbiting carbon observatory - 2&3 level 1B algorithm theoretical basis document. In: Algorithm Theoretical Basis Document D-55206. Jet Propulsion Laboratory January. URL. https://disc.gsfc.nasa.gov/datacollection/OCO3_L1B_Calibration_Early.html.

Fisher, J.B., Lee, B., Purdy, A.J., Halverson, G.H., Dohlen, M.B., Cawse-Nicholson, K., Wang, A., Anderson, R.G., Aragon, B., Arain, M.A., Baldocchi, D.D., Baker, J.M., Barral, H., Bernacchi, C.J., Bernhofer, C., Biraud, S.C., Bohrer, G., Brunsell, N., Cappelaere, B., Castro-Contreras, S., Chun, J., Conrad, B.J., Cremonese, E., Demarty, J., Desai, A.R., De Ligne, A., Foltýnová, L., Goulden, M.L., Griffis, T.J., Grünwald, T., Johnson, M.S., Kang, M., Kelbe, D., Kowalska, N., Lim, J.-H., Maïnassara, I., McCabe, M.F., Missik, J.E., Mohanty, B.P., Moore, C.E., Morillas, L., Morrison, R., Munger, J.W., Posse, G., Richardson, A.D., Russell, E.S., Ryu, Y., Sanchez-Azofeifa, A., Schmidt, M., Schwartz, E., Sharp, I., Šigut, L., Tang, Y., Hulley, G., Anderson, M., Hain, C., French, A., Wood, E., Hook, S., 2020. ECOSTRESS: NASA's next generation mission to measure evapotranspiration from the International Space Station. Water Resour. Res. 56 (4). https://doi.org/10.1029/2019WR026058. URL. https://agupubs.onlinelibrary.wiley.com/doi/abs/10.1029/2019WR026058.

Frankenberg, C., Butz, A., Toon, G., 2011. Disentangling chlorophyll fluorescence from atmospheric scatting effects in the O2 A band spectra of reflected sunlight. Geophys. Res. Lett. 38 (3).

Frankenberg, C., O'Dell, C., Berry, J., Guanter, L., Joiner, J., Köhler, P., Pollock, R., Taylor, T.E., 2014. Prospects for chlorophyll fluorescence remote sensing from the Orbiting Carbon Observatory-2. Remote Sens. Environ. 147, 1–12. https://doi.org/10.1016/j.rse.2014.02.007. URL. http://www.sciencedirect.com/science/article/pii/S0034425714000522.

Frey, M., Sha, M.K., Hase, F., Kiel, M., Blumenstock, T., Harig, R., Surawicz, G., Deutscher, N.M., Shiomi, K., Franklin, J.E., Bösch, H., Chen, J., Grutter, M., Ohyama, H., Sun, Y., Butz, A., Mengistu Tsidu, G., Ene, D., Wunch, D., Cao, Z., Garcia, O., Ramonet, M., Vogel, F., Orphal, J., 2019. Building the COllaborative Carbon Column Observing Network (COCCON): long-term stability and ensemble performance of the EM27/SUN Fourier transform spectrometer. Atmos. Meas. Tech. 12 (3), 1513–1530. https://doi.org/10.5194/amt-12-1513-2019. URL. https://www.atmos-meas-tech.net/12/1513/2019/.

Griffith, D.W., Deutscher, N.M., Velazco, V.A., Wennberg, P.O., Yavin, Y., Aleks, G.K., Washenfelder, R.a., Toon, G.C., Blavier, J.-F., Murphy, C., Jones, N., Kettlewell, G., Connor, B.J., Macatangay, R., Roehl, C., Ryczek, M., Glowacki, J., Culgan, T., Bryant, G., 2014a. TCCON Data from Darwin (AU), Release GGG2014R0, TCCON Data Archive, Hosted by CaltechDATA. https://doi.org/10.14291/tccon.ggg2014.darwin01.R0/1149290.

Griffith, D.W., Velazco, V.A., Deutscher, N.M., Murphy, C., Jones, N., Wilson, S., Macatangay, R., Kettlewell, G., Buchholz, R.R., Riggenbach, M., 2014b. TCCON Data from Wollongong (AU), Release GGG2014R0, TCCON Data Archive, Hosted by CaltechDATA. https://doi.org/10.14291/tccon.ggg2014.wollongong01.R0/1149291.

Hase, F., Blumenstock, T., Dohe, S., Gross, J., Kiel, M., 2014. TCCON Data from Karlsruhe (DE), Release GGG2014R1, TCCON Data Archive, Hosted by CaltechDATA. https://doi.org/10.14291/tccon.ggg2014.karlsruhe01.R1/1182416.

Heidinger, A., Botambekov, D., Walther, A., October 2016. A Naive Bayesian Cloud Mask Delivered to NOAA Enterprise, Algorithm Theoretical Basis Document. NOAA NESDIS Center for Satellite Applications and Research https://doi.org/10.5067/AJMZO5O3TGUR.

Iraci, L.T., Podolske, J., Hillyard, P.W., Roehl, C., Wennberg, P.O., Blavier, J.-F., Allen, N., Wunch, D., Osterman, G.B., Albertson, R., 2016. TCCON Data from Edwards (US), Release GGG2014R1, TCCON Data Archive, Hosted by CaltechDATA. https://doi.org/10.14291/tccon.ggg2014.edwards01.R1/1255068.

Janardanan, R., Maksyutov, S., Oda, T., Saito, M., Kaiser, J.W., Ganshin, A., Stohl, A., Matsunaga, T., Yoshida, Y., Yokota, T., 2016. Comparing GOSAT observations of localized CO_2 enhancements by large emitters with inventory-based estimates. Geophys. Res. Lett. 43 (7), 3486–3493. arXiv. https://agupubs.onlinelibrary.wiley.com/doi/pdf/10.1002/2016GL067843. https://doi.org/10.1002/2016GL067843 URL. https://agupubs.onlinelibrary.wiley.com/doi/abs/10.1002/2016GL067843.

Joyce, M.J., Dahl, L.B., Sposto, L., 2018. Advanced multi-mission operations system instrument toolkit: an open source instrument and small satellite operations toolkit. In: CubeSats and NanoSats for Remote Sensing II. Vol. 10769, 1076914. https://doi.org/10.1117/12.2320596.

Kawakami, S., Ohyama, H., Arai, K., Okumura, H., Taura, C., Fukamachi, T., Sakashita, M., 2014. TCCON Data from Saga (JP), Release GGG2014R0, TCCON Data Archive, Hosted by CaltechDATA. https://doi.org/10.14291/tccon.ggg2014.saga01.R0/1149283.

Kiel, M., O'Dell, C.W., Fisher, B., Eldering, A., Nassar, R., MacDonald, C.G., Wennberg, P.O., 2019. How bias correction goes wrong: measurement of XCO2 affected by erroneous surface pressure estimates. Atmos. Meas. Tech. 12 (4), 2241–2259. https://doi.org/10.5194/amt-12-2241-2019. URL. https://www.atmos-meas-tech.net/12/2241/2019/.

Ko, A., Maldague, P., Lam, D., Bui, T., McKinney, J., 2010. The evolvable advanced multi-Mission operations system (AMMOS): making systems interoperable. In: SpaceOps 2010 Conference, pp. 1–12. https://doi.org/10.2514/6.2010-2303.

Mandrake, L., Frankenberg, C., O'Dell, C., Osterman, G., Wennberg, P., Wunch, D., 2013. Semi-autonomous sounding selection for OCO-2. Atmos. Meas. Tech. 6, 2851–2864. https://doi.org/10.5194/amt-6-2851-2013.

Marchetti, Y., Rosenberg, R., Crisp, D., 2019. Classification of anomalous pixels in the focal plane arrays of Orbiting Carbon Observatory-2 and-3 via machine learning. In: Remote Sensing 11 (24), pp. 1–18. https://doi.org/10.3390/rs11242901. URL. https://www.mdpi.com/2072-4292/11/24/2901.

McKinney, C., Goodsall, T., Hoenk, M., Shelton, J., Rumney, K., Basset, C., Jeganathan, M., Moore, D., 2018. Context cameras for the Orbiting Carbon Observatory 3 (OCO-3) instrument. In: 2018 IEEE Aerospace Conference, Big Sky, MT. Institute of Electrical and Electronics Engineers, pp. 1–15. https://doi.org/10.1109/AERO.2018.8396759.

Morino, I., Yokozeki, N., Matzuzaki, T., Horikawa, M., 2014a. TCCON Data from Rikubetsu (JP), Release GGG2014R1, TCCON Data Archive, Hosted by CaltechDATA. https://doi.org/10.14291/tccon.ggg2014.rikubetsu01.R1/1242265.

Morino, I., Matsuzaki, T., Shishime, A., 2014b. TCCON Data from Tsukuba (JP), 125HR, Release GGG2014R1, TCCON Data Archive, Hosted by CaltechDATA. https://doi.org/10.14291/tccon.ggg2014.tsukuba02.R1/1241486.

Moy, A., Yelamanchili, A., Chien, S., Eldering, A., Pavlick, R., 2019. Automated scheduling for the orbiting carbon observatory 3 mission. In: Proceedings of 11th International Workshop on Planning and Scheduling for Space (IWPSS 2019), pp. 1–9.

Nassar, R., Hill, T.G., McLinden, C.A., Wunch, D., Jones, D.B.A., Crisp, D., 2017. Quantifying CO_2 emissions from individual power plants from space. Geophys. Res. Lett. 44 (19), 10,045–10,053. arXiv. https://agupubs.onlinelibrary.wiley.com/doi/pdf/10.1002/2017GL074702. https://doi.org/10.1002/2017GL074702 URL. https://agupubs.onlinelibrary.wiley.com/doi/abs/10.1002/2017GL074702.

Nelson, R.R., O'Dell, C.W., 2019. The impact of improved aerosol priors on near-infrared measurements of carbon dioxide. Atmos. Meas. Tech. 12 (3), 1495–1512. https://doi.org/10.5194/amt-12-1495-2019. URL. https://www.atmos-meas-tech.net/12/1495/2019/.

Notholt, J., Petri, C., Warneke, T., Deutscher, N.M., Buschmann, M., Weinzierl, C., Macatangay, R., Grupe, P., 2014. TCCON Data from Bremen (DE), Release GGG2014R0, TCCON Data Archive, Hosted by CaltechDATA. https://doi.org/10.14291/tccon.ggg2014.bremen01.R0/1149275.

OCO-2 Science Team, Gunson, M., Eldering, A., 2017a. OCO-2 Level 1B Calibrated, Geolocated Science Spectra. In: Retrospective Processing V8r. Goddard Earth Sciences Data and Information Services Center (GES DISC), Greenbelt, MD, USA.

https://doi.org/10.5067/1RJW1YMLW2F0. last accessed 5-June-2020.

OCO-2 Science Team, Gunson, M., Eldering, A., 2017b. OCO-2 Level 2 bias-corrected solar-induced fluorescence and other select fields from the IMAP-DOAS algorithm aggregated as daily files. In: Retrospective Processing V8r. Goddard Earth Sciences Data and Information Services Center (GES DISC), Greenbelt, MD, USA. https://doi.org/10.5067/AJMZO5O3TGUR. last accessed 5-June-2020.

OCO-2 Science Team, Gunson, M., Eldering, A., 2018. OCO-2 Level 2 bias-corrected XCO2 and other select fields from the full-physics retrieval aggregated as daily files. In: Retrospective processing V9r. Goddard Earth Sciences Data and Information Services Center (GES DISC), Greenbelt, MD, USA. https://doi.org/10.5067/W8QGIYNKS3JC. last accessed 5-June-2020.

O'Dell, C.W., Connor, B., Bösch, H., O'Brien, D., Frankenberg, C., Castano, R., Christi, M., Crisp, D., Eldering, A., Fisher, B., Gunson, M., McDuffie, J., Miller, C.E., Natraj, V., Oyafuso, F., Polonsky, I., Smyth, M., Taylor, T., Toon, G.C., Wennberg, P.O., Wunch, D., 2012. The ACOS CO$_2$ retrieval algorithm–Part 1: description and validation against synthetic observations. Atmos. Meas. Tech. 5, 99–121. https://doi.org/10.5194/amt-5-99-2012.

O'Dell, C., Taylor, T.E., Eldering, A., 2014. OCO-2 oxygen-A band cloud screening algorithm (ABO2). In: Algorithm Theoretical Basis Document D-81520. Jet Propulsion Laboratory URL. https://disc.gsfc.nasa.gov/datasets/OCO2_L1B_Science_8r/.

O'Dell, C.W., Eldering, A., Wennberg, P.O., Crisp, D., Gunson, M.R., Fisher, B., Frankenberg, C., Kiel, M., Lindqvist, H., Mandrake, L., Merrelli, A., Natraj, V., Nelson, R.R., Osterman, G.B., Payne, V.H., Taylor, T.E., Wunch, D., Drouin, B.J., Oyafuso, F., Chang, A., McDuffie, J., Smyth, M., Baker, D.F., Basu, S., Chevallier, F., Crowell, S.M.R., Feng, L., Palmer, P.I., Dubey, M., García, O.E., Griffith, D.W.T., Hase, F., Iraci, L.T., Kivi, R., Morino, I., Notholt, J., Ohyama, H., Petri, C., Roehl, C.M., Sha, M.K., Strong, K., Sussmann, R., Te, Y., Uchino, O., Velazco, V.A., 2018. Improved retrievals of carbon dioxide from orbiting carbon observatory-2 with the version 8 acos algorithm. Atmos. Meas. Tech. 11 (12), 6539–6576. https://doi.org/10.5194/amt-11-6539-2018. URL. https://www.atmos-meas-tech.net/11/6539/2018/.

Osterman, G., O'Dell, C., Eldering, A., Fisher, B., Crisp, D., Cheng, C., Frankenberg, C., Lambert, A., Gunson, M., Mandrake, L., Wunch, D., 2020. Orbiting Carbon Observatory-2 & 3. Data Product User's Guide, Operational Level 2 Data Versions 10 and Lite File Version 10 and VEarly. Jet Propulsion Laboratory, pp. 1–93. June, D-55208. URL. https://disc.gsfc.nasa.gov/datacollection/OCO3_L2_Standard_EarlyR.html.

Plascyk, J.A., 1975. The MK II Fraunhofer Line Discriminator (FLD-II) for airborne and orbital remote sensing of solar-stimulated luminescence. Opt. Eng. 14 (4), 339–346. https://doi.org/10.1117/12.7971842.

Pollard, D.F., Robinson, J., Shiona, H., 2019. Tccon Data From Lauder (nz), Release ggg2014.r0, TCCON Data Archive, Hosted by CaltechDATA. https://doi.org/10.14291/TCCON.GGG2014.LAUDER03.R0.

Reuter, M., Buchwitz, M., Schneising, O., Krautwurst, S., O'Dell, C.W., Richter, A., Bovensmann, H., Burrows, J.P., 2019. Towards monitoring localized CO$_2$ emissions from space: co-located regional CO$_2$ and NO$_2$ enhancements observed by the OCO-2 and S5P satellites. Atmos. Chem. Phys. 19 (14), 9371–9383. https://doi.org/10.5194/acp-19-9371-2019. URL. https://www.atmos-chem-phys.net/19/9371/2019/.

Schmit, T.J., Griffith, P., Gunshor, M.M., Daniels, J.M., Goodman, S.J., Lebair, W.J., 2017. A closer look at the ABI on the GOES-R series. Bull. Am. Meteorol. Soc. 98 (4), 681–698. https://doi.org/10.1175/BAMS-D-15-00230.1. https://doi.org/10.1175/BAMS-D-15-00230.1.

Sun, Y., Frankenberg, C., Wood, J.D., Schimel, D.S., Jung, M., Guanter, L., Drewry, D., Verma, M., Porcar-Castell, A., Griffis, T.J., Gu, L., Magney, T., Köhler, P., Evans, B., Yuen, K., 2017. OCO-2 advances photosynthesis observation from space via solar-induced chlorophyll fluorescence. Science 358 (6360), eaam5747. https://doi.org/10.1126/science.aam5747.

Sun, Y., Frankenberg, C., Jung, M., Joiner, J., Guanter, L., Köhler, P., Magney, T., 2018. Overview of the solar-induced chlorophyll fluorescence SIF from the Orbiting Carbon Observatory-2: Retrieval, cross-mission comparison, and global monitoring for GPP.

Remote. Sens. Environ. 209, 808–823. https://doi.org/10.1016/j.rse.2018.02.016.

Sussmann, R., Rettinger, M., 2014. TCCON Data from Garmisch (DE), Release GGG2014R0, TCCON Data Archive, Hosted by CaltechDATA. https://doi.org/10.14291/tccon.ggg2014.garmisch01.R0/1149299.

Taylor, T.E., O'Dell, C.W., Frankenberg, C., Partain, P.T., Cronk, H.Q., Savtchenko, A., Nelson, R.R., Rosenthal, E.J., Chang, A., Fisher, B.M., Osterman, G.B., Pollock, R.H., Crisp, D., Eldering, A., Gunson, M.R., 2016. Orbiting Carbon Observatory-2 (OCO-2) cloud screening algorithms: validation against collocated MODIS and CALIOP data. Atmos. Meas. Tech. 9, 973–989. https://doi.org/10.5194/amt-9-973-2016.

Te, Y., Jeseck, P., Janssen, C., 2014. TCCON Data from Paris (FR), Release GGG2014R0, TCCON Data Archive, Hosted by CaltechDATA. https://doi.org/10.14291/tccon.ggg2014.paris01.R0/1149279.

Vincent, M., 2018. Two geometric aspects of the orbiting carbon observatory 2 mission. In: Advances in the Astronautical Sciences. Vol. 143. pp. 2293–2304.

Warneke, T., Messerschmidt, J., Notholt, J., Weinzierl, C., Deutscher, N.M., Petri, C., Grupe, P., Vuillemin, C., Truong, F., Schmidt, M., Ramonet, M., Parmentier, E., 2014. TCCON Data from Orléans (FR), Release GGG2014R0, TCCON Data Archive, Hosted by CaltechDATA. https://doi.org/10.14291/tccon.ggg2014.orleans01.R0/1149276.

Wennberg, P.O., Wunch, D., Roehl, C., Blavier, J.-F., Toon, G.C., Allen, N., 2014a. TCCON Data from Caltech (US), Release GGG2014R1, TCCON Data Archive, Hosted by CaltechDATA. https://doi.org/10.14291/tccon.ggg2014.pasadena01.R1/1182415.

Wennberg, P.O., Roehl, C., Wunch, D., Toon, G.C., Blavier, J.-F., Washenfelder, R.a., Keppel-Aleks, G., Allen, N., Ayers, J., 2014b. TCCON Data from Park Falls (US), Release GGG2014R0, TCCON Data Archive, Hosted by CaltechDATA. https://doi.org/10.14291/tccon.ggg2014.parkfalls01.R0/1149161.

Wennberg, P.O., Wunch, D., Roehl, C., Blavier, J.-F., Toon, G.C., Allen, N., Dowell, P., Teske, K., Martin, C., Martin, J., 2016. TCCON Data from Lamont (US), Release GGG2014R1, TCCON Data Archive, Hosted by CaltechDATA. https://doi.org/10.14291/tccon.ggg2014.lamont01.R1/1255070.

Wu, D., Lin, J.C., Oda, T., Kort, E.A., 2020. Environ. Res. Lett. 15 (3). https://doi.org/10.1088/1748-9326/ab68eb. 035004. URL https://doi.org/10.1088.

Wunch, D., Toon, G.C., Blavier, J.-F.L., Washenfelder, R.A., Notholt, J., Connor, B.J., Griffith, D.W.T., Sherlock, V., Wennberg, P.O., 2011. The Total carbon column observing network. Philos. Trans. R. Soc. A Math. Phys. Eng. Sci. 369. https://doi.org/10.1098/rsta.2010.0240.

Wunch, D., Toon, G.C., Sherlock, V., Deutscher, N.M., Liu, C., Feist, D.G., Wennberg, P.O., 2015. Documentation for the 2014 TCCON Data Release, TCCON Data Archive, Hosted by CaltechDATA. https://doi.org/10.14291/TCCON.GGG2014.DOCUMENTATION.R0/1221662.

Wunch, D., Wennberg, P.O., Osterman, G., Fisher, B., Naylor, B., Roehl, C.M., O'Dell, C., Mandrake, L., Viatte, C., Kiel, M., 2017. Comparisons of the Orbiting Carbon Observatory-2 (OCO-2) XCO$_2$ measurements with TCCON. Atmos. Meas. Tech. 10 (6), 2209.

Yang, X., Shi, H., Stovall, A., Guan, K., Miao, G., Zhang, Y., Zhang, Y., Xiao, X., Ryu, Y., Lee, J.-E., 2018. Fluospec 2—an automated field spectroscopy system to monitor canopy solar-induced fluorescence. Sensors 18 (7), 2063.

Ye, X., Lauvaux, T., Kort, E.A., Oda, T., Feng, S., Lin, J.C., Yang, E.G., Wu, D., 2020. Constraining fossil fuel CO$_2$ emissions from urban area using OCO-2 observations of total column CO$_2$. J. Geophys. Res.-Atmos. 125 (8). https://doi.org/10.1029/2019JD030528. URL. https://agupubs.onlinelibrary.wiley.com/doi/abs/10.1029/2019JD030528.

Yu, S., Rosenberg, R., Bruegge, C., Chapsky, L., Fu, D., Lee, R., Taylor, T.E., Cronk, H., O'Dell, C., Angal, A., Xiong, X., Crisp, D., Eldering, A., 2020. Stability assessment of OCO-2 radiometric calibration using Aqua MODIS. Remote Sens. 12 (8), 1269. https://doi.org/10.3390/rs12081269.

Zheng, T., Nassar, R., Baxter, M., 2019. Estimating power plant CO$_2$ emission using OCO-2 XCO$_2$ and high resolution WRF-Chem simulations. Environ. Res. Lett. 14 (8), 085001. https://doi.org/10.1088/1748-9326/ab25ae.